# SPACE-SHUTTLE WINDWARD SURFACE LAMINAR VISCOUS SHOCK-LAYER FLOWS IN EQUILIBRIUM AIR AT HIGH ANGLES-OF-ATTACK

by

Rajiv R Thareja

Thesis submitted to the Graduate Faculty of the

Virginia Polytechnic Institute and State University

in partial fulfillment of the requirements for the degree of

MASTER OF SCIENCE

in

Aerospace Engineering

APPROVED:

C.H. Lewis

W.L. Hallauer, Jr.

D.M. Rooney

January, 1982
Blacksburg, Virginia

SPACE-SHUTTLE WINDWARD SURFACE LAMINAR
VISCOUS SHOCK-LAYER FLOWS IN EQUILIBRIUM AIR
AT HIGH ANGLES-OF-ATTACK

by

Rajiv R Thareja

(ABSTRACT)

A recently developed viscous shock-layer method (VSL81) has been applied to predict laminar viscous flows over the windward surface of a shuttle-like vehicle with a perfect gas and an equilibrium air model at high angles-of-attack to simulate reentry conditions. The predictions of wall pressure and heat-transfer data compare well with the limited experimental data available requiring relatively short computing times compared to parabolized Navier-Stokes (PNS) methods. Velocity, pressure and enthalpy profiles are compared at some stations on the body. This method can be used to predict viscous flows over general lifting bodies during reentry.

ACKNOWLEDGEMENTS

The author expresses his thanks to Dr. Clark H. Lewis, his major advisor for conceiving and supporting this thesis, to Dr. W.L. Hallauer, Jr. and Dr. D.M. Rooney for serving as members of the advisory committee, and to Dr. K.Y. Szema for his continued help and suggestions.

TABLE OF CONTENTS

# LIST OF TABLES

Table

LIST OF FIGURES

## NOMENCLATURE

| | |
|---|---|
| $a$ | acceleration |
| $C^*_p$ | specific heat at constant pressure |
| $\hat{e}_i$ | unit vector of a general orthogonal coordinate system |
| $f$ | body force |
| $g$ | determinant of coordinate metric tensor |
| $\vec{g}^i$ | vector orthogonal to $\vec{g}_j$ and $\vec{g}_k$ ; $i \neq j$, $i \neq k$ |
| $g_{ij}$ | coordinate metric tensor, $\vec{g}_i \cdot \vec{g}_j$ ; $i,j = 1,2,3$ |
| $g^{ij}$ | $\vec{g}^i \cdot \vec{g}^j$ ; $i,j = 1,2,3$ |
| $\vec{g}_1$ | vector in $\xi_1$ (streamwise) direction |
| $\vec{g}_2$ | vector in $\xi_2$ (normal) direction |
| $\vec{g}_3$ | vector in $\xi_3$ (circumferential) direction |
| $H$ | total enthalpy, $H^*/U^{*2}_\infty$ |
| $h$ | static enthalpy, $h^*/U^{*2}_\infty$ |
| $\bar{H}$ | heat-transfer coefficient, $Q_w/(T_o-T_w)$, $Btu/ft^2\text{-sec-R}$ |
| $M_\infty$ | freestream Mach number |
| $nsh$ | shock standoff distance, $nsh^*/R_n^*$ |
| $p$ | pressure, $p^*/p_{ref}$ |
| $p_{ref}$ | reference pressure , $\rho^*_\infty U^{*2}_\infty$ |
| $Pr$ | Prandtl number |
| $Q_w$ | convective heat-transfer rate, $Btu/ft^2\text{-sec}$ |
| $r$ | local body radius |
| $R_n^*$ | body nose radius of curvature |

| | |
|---|---|
| $Re_\infty$ | freestream unit Reynolds number, $ft^{-1}$ |
| s | surface distance coordinate measured along the body from nose-tip, $s^*/R_n^*$ |
| T | temperature, $T^*/T^*_{ref}$ |
| $T^*_{ref}$ | reference temperature, $(\gamma - 1) M_\infty T_\infty$ or $U^{*2}_\infty/C^*_P$ |
| $U^*_\infty$ | dimensional freestream velocity |
| u,v,w | streamwise, normal and crossflow velocity components nondimensionalizesd by the freestream velocity $U^*_\infty$ |
| V | local velocity vector, $u\vec{g_1} + v\vec{g_2} + w\vec{g_3}$ |
| z,r,$\phi$ | cylindrical coordinates |
| $\alpha$ | angle of attack, degree |
| $\gamma$ | ratio of specific heats |
| $\epsilon$ | Reynolds number parameter, $\epsilon^2 = \mu^*_{ref} / \rho^*_\infty U^*_\infty R_n^*$ |
| $\mu$ | viscosity, $\mu^*/\mu^*_{ref}$ |
| $\mu^*_{ref}$ | reference viscosity, $\mu^*(T^*_{ref})$ |
| $\tau$ | shear stress |
| $\xi_1, \xi_2, \xi_3$ | computational coordinates |
| $\rho$ | density, $\rho^*/\rho^*_\infty$ |
| $\{^i_{jk}\}$ | Christoffel symbol of the second kind (Appendix B), $\frac{1}{2}\sum_m g^{im}\left[\frac{\partial g_{mk}}{\partial \xi_j} + \frac{\partial g_{mj}}{\partial \xi_k} - \frac{\partial g_{jk}}{\partial \xi_m}\right]$ |

Subscript

| | |
|---|---|
| B | Bade |
| C | Cohen |

| | |
|---|---|
| w | wall value |
| o | stagnation condition |
| ∞ | freestream value |

Superscript

| | |
|---|---|
| * | dimensional quantity |

# Chapter I

## INTRODUCTION

Numerous methods exist to analyse viscous flows over axisymmetric bodies. Most reentry vehicles, though, are far from axisymmetric. Complex geometries present new difficulties in geometry definitions, grid generation and analysis of flow around such vehicles, of which the shuttle orbiter is a classical example.

Reentry vehicles operate through a wide range of flow conditions. The complex hypersonic flowfield is bounded by the body and the bow shock. Due to the high angles-of-attack usually present, crossflow separation may be present, and the viscous effects may predominate over the entire flowfield. For very low Reynolds numbers, the full Navier-Stokes equations must be considered. These equations are elliptic in all three space directions, and a numerical solution is difficult and requires large computing times and storage. For moderately high values of Reynolds numbers there is no need to solve the full Navier-Stokes equations. The classical approach to solving such a flowfield is to divide the flow into an outer inviscid region and a viscous boundary-layer region. The wall values of the inviscid solution are used as edge conditions for the viscous calcula-

tions. This approach works well for low altitude supersonic high Reynolds number flows in which the boundary-layer is thin compared to the shock-layer thickness. At higher altitudes, the boundary-layer assumptions become increasingly inaccurate as the Reynolds number decreases. At hypersonic low Reynolds number conditions, the viscous layer may extend right up to the shock, especially in the stagnation region, and the displacement effect must be modeled by interacting the viscous calculations with the inviscid solution. Another problem with this approach is determining the edge conditions for the boundary-layer calculations. Methods such as streamline-tracking and entropy-layer swallowing have been used to help solve this problem. The parabolized Navier-Stokes (PNS) approach uses a parabolic approximation in the streamwise direction, thus enabling a wide variety of problems to be solved by using a streamwise marching scheme. The PNS method involves large matrix solutions due to its elliptic nature in the crossflow direction, and the computing times are still quite large. The viscous shock-layer (VSL) equations treat the entire flowfield uniformly with one set of equations and have no problems with displacement effects. The edge conditions for the shock-layer approach are easily obtained from the Rankine-Hugoniot equations. Another major advantage of the shock-layer approach is that

the equations are parabolic in both the streamwise and crossflow directions and can be solved easily by direct, highly efficient finite-difference methods. Since the crossflow momentum equation is parabolic, the crossflow separated region on the leeward side cannot be treated. Nevertheless, the solution for the windward region up to crossflow separation is accurate and the computing times are relatively small. As a result, the viscous shock-layer method treats all higher-order boundary-layer effects (displacement, vorticity interaction, longitudinal and transverse curvature, including proper matching conditions) in a straight-forward and consistent manner, making the viscous shock-layer approach especially attractive for design studies.

In recent years, the viscous shock-layer equations have been applied to a wide range of problems by a number of investigators. Davis[1] solved the shock-layer equations for laminar, perfect gas flows over analytical bodies such as hyperboloids for which the pressure distributions were nearly Newtonian. Whitehead and Davis[2] considered the problem of inert gas injection through porous walls of analytic shapes. Miner and Lewis[3-4] extended the method for a seven-species air mixture with finite-rate chemical reactions over non-analytic blunt bodies for which the shock shape differed

from the body shape. They used the viscous shock-layer equations to obtain a solution for the windward plane of the shuttle. Anderson and Moss[7] added turbulence to the shock-layer equations for axisymmetric blunt bodies. Eaton and Larson[8] and Eaton and Kaestner[9] extended the equations to consider the windward and leeward planes of symmetry on bodies at angle-of-attack. Srivastava, Werle and Davis[10] treated the problem of the curvature discontinuity on a sphere-cone and applied an ADI technique to iterate on the shock standoff distance. Waskiewicz and Lewis[11] used the viscous shock-layer approach to provide a blunt-body solution for a PNS method for sphere-cones at large angles-of-attack. Waskiewicz, Murray and Lewis[12] developed a coupling scheme for the continuity and normal momentum equations to improve the solution. Murray and Lewis[13-14] developed the viscous shock-layer equations for three-dimensional bodies at large angles-of-attack and substantiated this development with a wide range of conditions.[15] Murray and Lewis[16] added the effects of heat and/or mass transfer by modifying the boundary conditions of the viscous shock-layer equations. Gogineni, Murray and Lewis[17] computed the aerodynamic coefficients of slender cones with mass-transfer and low Reynolds numbers to study the limits of the range of the viscous shock-layer applicability. Tree, Melson and Lewis[18]

used non-equilibrium chemistry in the viscous shock-layer solution for the NASA Jovian entry probe, a 45 degree spherically blunted cone. Gogineni and Lewis[19] combined the advantages of both the VSL and PNS methods to develop a hybrid VSLPNS code, in which the VSL solution was obtained up to crossflow separation, and the flowfield data prior to crossflow separation was saved and used to start a PNS solution on the remaining lee side. Szema and Lewis[20] extended the VSL3D method to include transitional and/or turbulent flows. A two-layer eddy-viscosity model proposed by Cebeci[21] and the transition model developed by Dhawan and Narasimha[22] were included in their analysis, which was applicable for a perfect gas only. Thareja, Szema and Lewis[23] modified the VSL3D analysis for axisymmetric flows to include the effects of air in chemical equilibrium for which the thermodynamic and transport properties of air are obtained from tables or from curve-fits. Szema and Lewis[24-25] developed the viscous shock-layer equations for a nonorthogonal, body-oriented coordinate system in which the three velocity components were defined in the nonorthogonal coordinate directions which made it possible to solve for a non-spherical nose and treat general lifting bodies at high angles-of-attack in a perfect gas.

The purpose of this work is to apply the method of Szema and Lewis[24-25] to analyse the flow over the windward surface of a shuttle-like vehicle for perfect gas and equilibrium air in typical reentry conditions.

Calculations have been made for a perfect gas model at two angles-of-attack and the predictions are compared with inviscid solutions and some experimental data from the Arnold Engineering Development Center (AEDC) where tests were conducted on models of the shuttle orbiter[26-28] in tunnels at the von Karman Gas Dynamics Facility to simulate reentry conditions. Since experimental data were not available for the equilibrium air case, the computed results are compared with the inviscid equilibrium air solution. Profiles normal to the body in the windward plane are compared for some stations.

Chapter 2 presents the analysis of the problem and the solution procedure used in this method. Chapter 3 discusses the results obtained for the sample cases, while Chapter 4 stresses the main conclusions and recommendations for further study. The derivation of the viscous shock-layer equations for laminar flow from the steady Navier-Stokes equations in a general non-orthogonal coordinate system is given in Appendix A. The grid generation procedure is given in more detail in Appendix B.

## Chapter II

## ANALYSIS

For a general three-dimensional vehicle like the shuttle orbiter, an accurate geometry definition is a prerequisite for any analysis of flow over the vehicle. Using the method developed by Vachris and Yaeger[29] called QUICK, the geometry of the orbiter was represented by a series of analytical functions in a cylindrical coordinate system ($z, r, \phi$). A moving map axis was necessary to define the center of the coordinate system as a function of z to ensure a unique value of r for a given angle $\phi$ around the body. The primary region of interest was the windward surface. Using QUICK, two versions of the space shuttle orbiter were obtained. The first conformed as close as possible to the actual vehicle (Figure 1), with the exception that the canopy and tail-sections were removed. The second geometry had the same lower surface and upper-symmetry plane profile (Figure 2) . For both geometries the wing was swept back to 55 degrees from the design value of 45 degrees to avoid an imbedded subsonic region at the wing-body juncture which cannot be handled by the inviscid method used here. However, the region between the strake and wing leading edge and the upper-symmetry plane surface was filled in with elliptic

curves. Nevertheless, the geometry is a good representation of the space shuttle up to about $\phi$ = 80 degrees. Because the region of interest was the windward surface only, the latter geometry version has been used in this analysis. Large changes in transverse curvature are present at the wing leading edge as seen in cross-sections of the modified shuttle-like geometry (Figure 3). It must also be mentioned here that the location of the transverse curvature discontinuity moves from $\phi$ = 65 degrees to about $\phi$ = 80 degrees in the latter half of the vehicle.

An inviscid time-dependent method called BLUNT[30] developed by Moretti was used to obtain a solution over the nonspherical nose and an initial data plane was obtained at a station (Z/Rn=3), where the axial mach number was entirely supersonic. Then an inviscid marching method STEIN developed by Marconi and Yaeger[31] was used to solve the inviscid flowfield over the entire shuttle-like geometry downstream of the supersonic initial data plane.

## 2.1 GOVERNING EQUATIONS

The basic equations are derived from the steady Navier-Stokes equations expressed in general body-oriented (Figure 4) tensor form. One of the coordinates, $\xi_1$, is chosen in the general axial direction, another $\xi_2$, in a direction normal to the body, and the third, $\xi_3$, around the body. The coordinate system requires orthogonality only at the body surface. The normal velocity v and the normal coordinate $\xi_2$ are assumed to be of order $\epsilon$, and all terms which are of higher order than $\epsilon$ are neglected. These equations are parabolic in the streamwise and crossflow directions. The methods of obtaining these equations are discussed by Szema and Lewis.[24-25] The nondimensional form of the viscous shock-layer equations (Appendix A) that are applicable in the present study can be written as follows :

Continuity Equation:

$$\frac{\partial}{\partial \xi_1}\left(\rho u g^{1/2}\right) + \frac{\partial}{\partial \xi_2}\left(\rho v g^{1/2}\right) + \frac{\partial}{\partial \xi_3}\left(\rho w g^{1/2}\right) = 0 \qquad (1)$$

$\xi_1$-Momentum Equation:

$$\rho u \frac{\partial u}{\partial \xi_1} + \rho v \frac{\partial u}{\partial \xi_2} + \rho w \frac{\partial u}{\partial \xi_3} + \rho \left[ u^2 \begin{Bmatrix} 1 \\ 1 \; 1 \end{Bmatrix} + 2uv \begin{Bmatrix} 1 \\ 1 \; 2 \end{Bmatrix} + 2uw \begin{Bmatrix} 1 \\ 1 \; 3 \end{Bmatrix} + v^2 \begin{Bmatrix} 1 \\ 2 \; 2 \end{Bmatrix} + 2vw \begin{Bmatrix} 1 \\ 2 \; 3 \end{Bmatrix} + w^2 \begin{Bmatrix} 1 \\ 3 \; 3 \end{Bmatrix} \right]$$

$$+ \quad \frac{g_{22}}{g}\left[g_{33}\ \frac{\partial p}{\partial \xi_1} - g_{13}\ \frac{\partial p}{\partial \xi_3}\right]$$

$$= \quad \frac{\epsilon^2}{g_{22}}\left[\frac{\partial \mu}{\partial \xi_2}\ \frac{\partial u}{\partial \xi_2} + \mu\ \frac{\partial^2 u}{\partial \xi_2^2}\right] \tag{2}$$

$\xi_2$ -Momentum Equation:

$$\rho u\ \frac{\partial v}{\partial \xi_1} + \rho v\ \frac{\partial v}{\partial \xi_2} + \rho w\ \frac{\partial v}{\partial \xi_3} + \rho\left[u^2\left\{\begin{matrix}2\\1\ 1\end{matrix}\right\} + 2uv\left\{\begin{matrix}2\\1\ 2\end{matrix}\right\}\right.$$

$$\left. + 2uw\left\{\begin{matrix}2\\1\ 3\end{matrix}\right\} + v^2\left\{\begin{matrix}2\\2\ 2\end{matrix}\right\} + 2vw\left\{\begin{matrix}2\\2\ 3\end{matrix}\right\} + w^2\left\{\begin{matrix}2\\3\ 3\end{matrix}\right\}\right]$$

$$+ \quad \frac{1}{g_{22}}\frac{\partial p}{\partial \xi_2} = 0 \tag{3}$$

$\xi_3$ -Momentum Equation:

$$\rho u\ \frac{\partial w}{\partial \xi_1} + \rho v\ \frac{\partial w}{\partial \xi_2} + \rho w\ \frac{\partial w}{\partial \xi_3} + \rho\left[u^2\left\{\begin{matrix}3\\1\ 1\end{matrix}\right\} + 2uv\left\{\begin{matrix}3\\1\ 2\end{matrix}\right\}\right.$$

$$\left. + 2uw\left\{\begin{matrix}3\\1\ 3\end{matrix}\right\} + v^2\left\{\begin{matrix}3\\2\ 2\end{matrix}\right\} + 2vw\left\{\begin{matrix}3\\2\ 3\end{matrix}\right\} + w^2\left\{\begin{matrix}3\\3\ 3\end{matrix}\right\}\right]$$

$$+ \quad \frac{g_{22}}{g}\left[g_{11}\ \frac{\partial p}{\partial \xi_3} - g_{13}\ \frac{\partial p}{\partial \xi_1}\right]$$

$$= \quad \frac{\epsilon^2}{g_{22}}\left[\frac{\partial \mu}{\partial \xi_2}\ \frac{\partial w}{\partial \xi_2} + \mu\ \frac{\partial^2 w}{\partial \xi_2^2}\right] \tag{4}$$

Energy Equation:

$$\rho u \frac{\partial h}{\partial \xi_1} + \rho v \frac{\partial h}{\partial \xi_2} + \rho w \frac{\partial h}{\partial \xi_3} - \left[ u \frac{\partial p}{\partial \xi_1} + v \frac{\partial p}{\partial \xi_2} + w \frac{\partial p}{\partial \xi_3} \right]$$

$$= \frac{\epsilon^2}{g_{22}} \left[ \frac{\partial}{\partial \xi_2} \left( \frac{\mu}{Pr} \right) \frac{\partial h}{\partial \xi_2} + \frac{\mu}{Pr} \frac{\partial^2 h}{\partial \xi_2^2} \right]$$

$$+ \frac{\epsilon^2 \mu}{g_{22}} \left[ g_{11} \left( \frac{\partial u}{\partial \xi_2} \right)^2 + 2 g_{13} \frac{\partial u}{\partial \xi_2} \frac{\partial w}{\partial \xi_2} \right.$$

$$\left. + g_{33} \left( \frac{\partial w}{\partial \xi_2} \right)^2 \right] \qquad (5)$$

In the governing equation $\left\{ \begin{matrix} i \\ j\ k \end{matrix} \right\}$ are the Christoffel symbols of the second kind, and the metric $g_{ij}$ can be obtained numerically from the grid generation procedure (Appendix B).

In these equations, u, v and w are the tensor velocity components. The physical components are obtained by multiplying the respective term by $\sqrt{g_{ii}}$ .

For a perfect gas the Prandtl number is assumed constant everywhere and is a function of pressure and enthalpy for a gas in chemical equilibrium.

Equation of State:

$$\rho = \rho (p,h) \qquad (6)$$

For a perfect gas, equation (6) has the analytical form

$$\rho = \gamma p / [(\gamma - 1) T] \qquad (7)$$

where $\gamma$ is the ratio of specific heats. For air in chemical equilibrium, the functional relation may be given by a table or an approximate analytical expression (curve-fit); the forms of which are given in detail in Section 2.3.

## 2.2 BOUNDARY CONDITIONS

In order to solve the above set of governing equations, it is essential to specify appropriate boundary conditions at the body surface and at the shock. At the body surface (wall), no-slip and no-temperature jump conditions were used. Consequently, at the wall

$$u_w = v_w = w_w = 0, \text{ and}$$
$$h_w \text{ or } q_w \text{ specified.} \qquad (6)$$

The conditions immediately behind the shock were obtained by using the Rankine-Hugoniot relations.

## 2.3 THERMODYNAMIC AND TRANSPORT PROPERTIES

For a perfect gas, the thermodynamic properties for specific heat and enthalpy can be expressed as

$$C_p = \gamma R / ( \gamma - 1 ) \quad \text{and} \quad h = C_p T.$$

The viscosity is calculated from Sutherland's viscosity law:

$$\mu = 2.27 \text{ E-8 } T^{3/2} / ( T + 198.6) \text{ slug/ft-sec}$$

The Prandtl number is assumed constant everywhere.

For air in chemical equilibrium a table look-up procedure or curve-fit data is used to provide the thermodynamic and transport properties as a function of pressure and enthalpy.

Table Look-Up

A two-dimensional table was generated for the properties using the method developed by Miner, Anderson and Lewis.[32] For a given pressure and temperature, the enthalpy and density are determined using the reservoir calculations of Lordi, Mates and Moselle.[33] The viscosity is obtained from curve-fits from the Wilke semi-empirical formula, while the Prandtl number is obtained by interpolation of the Hansen[34] data.

Cohen curve-fits

Curve-fit data are based on Cohen's fit[35] of Hansen's tables for the transport properties and Moeckel's tables[36] for the thermodynamic properties of equilibrium air.

Density: The enthalpy dependence of the density is given by the curve-fit:

$$\frac{\rho_E}{\rho} = 1.0 - 1.0477 \left[ 1.0 - \left( \frac{h}{h_E} \right)^{0.6123} \right]$$

This fit is reasonably good for the enthalpy range

$0.0152 \leq h/h_E \leq 2.0$. The maximum deviation in this range is about 25 percent at low enthalpy, and the average deviation for all data is about six percent.

The pressure dependence is given by the following:

$$\frac{\rho_E}{\rho_C} = 0.0294 \left(\frac{p}{p_C}\right)^{0.965}$$

This fit has a deviation of less than one-half percent over the range of pressure $1.E\text{-}4 \leq p/p_C \leq 10.0$.

Viscosity: The enthalpy dependence for the viscosity-density product is given by the curve-fit:

$$\frac{\rho_E \mu_E}{\rho \mu} = 1.0 - 1.0213 \left[1.0 - \left(\frac{h}{h_E}\right)^{0.3329}\right]$$

This fit has considerably better agreement than that for the density. The maximum deviation over the enthalpy range $0.0152 \leq h/h_E \leq 2.0$ is about 8 percent, and the average deviation is about three percent.

For the pressure dependence the following was used:

$$\frac{\rho_E \mu_E}{\rho_C \mu_C} = 0.225 \left(\frac{p}{p_C}\right)^{0.992}$$

This fit too has a deviation of about one-half percent.

Prandtl Number: The dependence of Prandtl number on pressure is neglected, and its variation with enthalpy (Figure 5) is assumed to be a fit of Hansen's data.[34] A precondition for the validity of an effective Prandtl number is that the gas must be in local thermodynamic equilibrium.

Bade curve-fits

The density curve-fits from Cohen are not in good agreement at low enthalpy. Better values of density are obtained using curve-fits suggested by Bade[37]:

$$\left(\frac{\rho}{\rho_B}\right) = \left(\frac{p}{p_B}\right)\left(\frac{h}{h_B}\right)^{-x}$$

where

$$x = 0.70 + 0.04 \log_{10} (p/p_B) \quad \text{if } 31.9 \leq h/RTo \leq 480$$

$$x = 0.94 \quad \text{if } h/RTo \leq 31.9$$

The fits have a maximum deviation of seven percent.

The viscosity and Prandtl number are then evaluated as in the Cohen curve-fits.

Reference Quantities in Curve-fits

The following reference quantities were used in the calculations:

$$h_E = 2.119\ E8\ ft^2/sec^2 = 8465\ Btu/lbm$$

$p_c$ = 1.0 atm

$\mu_c$ = 3.584 E-7 slugs/ft-sec

$\rho_c$ = 2.498 E-3 slugs/ft$^3$

$\rho_B$ = 0.01 lb/ft$^3$

$h_B$ = 1080 Btu/lb = 31.9 RTo

$p_B$ = 1.0 atm

## 2.4 COORDINATE GENERATION

Based on the general curvilinear coordinate governing equations, a body-oriented nonorthogonal coordinate system is constructed. This is first done on the surface of the body, where $\xi_2 = 0$, and then extended to points away from the surface of the body. The coordinate system requires orthogonality only at the body surface. At all points the $\xi_2$ coordinate is orthogonal to both $\xi_1$ and $\xi_3$. The approach used is an extension of that presented by Blottner,[38] and a detailed discussion of a similar procedure can be found in References 14 and 39.

## 2.5 SHOCK-SHAPE CALCULATIONS

For the viscous shock-layer method, an initial shock shape is necessary for which an inviscid shock shape can be used as an initial guess. If this inviscid shock shape is not too different from the viscous shock shape, global iterations can be avoided, otherwise it may be necessary to iterate on the shock shape computed by the viscous shock-layer method.

Using QUICK,[29] normals to the body were constructed, and the intersections of these normals with the three-dimensional inviscid shock surface were computed to give the shock standoff distance in each plane as a function of z and s, the surface distance in that plane. The shock standoff distance, the derivative $\partial nsh/\partial s$ and the shock angle $\sigma$ were smoothed by using a four-point Lagrangian walking least-squares fit.

## 2.6 METHOD OF SOLUTION

Davis[1] presented an implicit finite-difference method to solve the viscous shock-layer equations for axially symmetric flows. Murray and Lewis[13-14] extended the method to three-dimensional high angle-of-attack conditions. The present method of solution has been developed by Szema and Lewis.[25] Therefore, only an overview of the solution procedure is presented.

The $\xi_1$-momentum, $\xi_3$-momentum and energy equations are written in the standard form

$$A_0 \frac{\partial^2 W}{\partial \xi_2^2} + A_1 \frac{\partial W}{\partial \xi_2} + A_2 W + A_3 + A_4 \frac{\partial W}{\partial \xi_1} + A_5 \frac{\partial W}{\partial \xi_3} = 0$$

where W is the independent variable.

The derivatives are evaluated by the finite-difference expressions used by Frieders and Lewis[40].

$$\frac{\partial^2 W}{\partial \xi_2^2} = \frac{2[W_{2,j+1} - (1+k)\, W_{2,j} + kW_{2,j-1}]}{(\xi_{2,j+1} - \xi_{2,j})^2 + k(\xi_{2,j} - \xi_{2,j-1})^2}$$

$$\frac{\partial W}{\partial \xi_2} = \frac{[W_{2,j+1} - (1-k^2)\, W_{2,j} - k^2 W_{2,j-1}]}{(\xi_{2,j+1} - \xi_{2,j}) + k^2(\xi_{2,j} - \xi_{2,j-1})}$$

$$W = W_{2,j}$$

$$\frac{\partial W}{\partial \xi_1} = [W_{2,j} - W_{3,j}]/\Delta\xi_1$$

$$\frac{\partial W}{\partial \xi_3} = [(W_{4,j} - W_{3,j}) + (W_{2,j} - W_{1,j})]/2\Delta\xi_3$$

where $k = (\xi_{2,j+1} - \xi_{2,j})/(\xi_{2,j} - \xi_{2,j-1})$

The subscripts 1, 2, 3 and 4 in the above finite-difference expressions for the derivatives represent grid points in the computational domain as shown in Figure 6.

With these expressions, the parabolic equation in a finite-difference form is obtained as

$$\bar{A}_j W_{2,j-1} + \bar{B}_j W_{2,j} + \bar{C}_j W_{2,j+1} = \bar{D}_j$$

The solution to this equation has been developed by Richtmyer, and the general solution is

$$W_{2,j} = E_j W_{2,j+1} + F_j$$

where

$$E_j = -\bar{C}_j / [\bar{A}_j E_{j-1} + \bar{B}_j], \text{ and}$$

$$F_j = (\bar{D}_j - \bar{A}_j F_{j-1}) / (\bar{A}_j E_{j-1} + \bar{B}_j)$$

The boundary conditions are specified by defining $E_1$ and $F_1$ as $E_1 = 0$ and $F_1 = W_w$ when the wall values are known and as $E_1 = 1$ and $F_1 = 0$ when $(\partial W / \partial \xi_2)_w = 0$. The continuity and $\xi_2$-momentum equations are solved by a similar method, but they are coupled together. The continuity equation is integrated to give the shock standoff distance.

The solution begins on the blunt nose by obtaining an approximate stagnation solution in a wind-fixed coordinate system. At a specified location the data are rotated and an initial data plane formed. The three-dimensional solution begins on the windward plane and marches around the body obtaining a converged solution in each $\phi$ plane. After a com-

plete sweep in the $\xi_3$ direction, the procedure then steps downstream in $\xi_1$ and then begins the next $\phi$ sweep. At each point the equations are solved in the following order:
(i) $\xi_3$-momentum gives w, (ii) energy gives h or T,
iii) $\xi_1$-momentum gives u, (iv) integration of continuity gives nsh, and (v) coupled continuity and $\xi_2$-momentum gives p and v.

# Chapter III

# RESULTS AND DISCUSSION

Three cases are presented to substantiate the recently developed VSL81 code. The freestream conditions for all three cases are summarized in Table 1.

Case A was for the shuttle orbiter at an angle-of-attack of 25 degrees with a perfect gas model. Case B was nearly the same Mach number, but the freestream pressure was much higher and the angle-of-attack was 44 degrees with a perfect gas model. Finally, Case C was a slightly higher Mach number at an angle-of-attack of 25 degrees with an equilibrium air model (Bade curve-fits). This Mach number was not high enough to bring out many of the equilibrium effects.

## Case A

The inviscid and viscous shock standoff distance for various planes around the body indicate a slightly thinner shock-layer for the viscous case (Figure 7).

The wall pressure in the windward symmetry plane for the viscous and the inviscid STEIN[31] solutions are in good agreement (Figure 8). At an axial station of about Z/L = 0.75, there is a slight drop in both the inviscid and viscous wall pressure predictions due to an expansion region on

the vehicle. The predictions for the viscous shock-layer solution for other planes are shown in Figure 9. On much of the windward side, the body is relatively flat and the transverse curvature changes rapidly between $\phi$ = 65 and 80 degrees depending on the axial distance. Over most of the lower surface, due to the flatness, the wall pressure is nearly constant, increasing a little around the wing leading edge and then rapidly decreasing beyond that.

The heat-transfer rate compares very well with experimental data obtained by Martindale[27] and Herrera[28] in an AEDC wind tunnel for the windward symmetry plane (Figure 10). Hardly any experimental data are available off this plane, so the viscous shock-layer results around the body could not be substantiated. Due to the rapid change in the transverse curvature at the wing leading edge, there was an increase in the heat-transfer compared to the windward value (Figure 11). After the wing leading edge, the heat-transfer dropped off rapidly around the body. It should be noted that due to the shift of the wing leading edge from $\phi$ = 65 to 80 degrees along the axial direction, the heat-transfer predictions for $\phi$ = 60 degrees decrease while those for $\phi$ = 80 degrees increase very rapidly after Z/L = 0.6.

The u-velocity profiles normal to the body in the windward symmetry plane for two axial stations are shown in Fig-

ure 12. The pressure profiles show a nearly uniform pressure across the shock-layer (Figure 13). The enthalpy profiles indicate a large gradient at the wall due to the low value of the wall temperature (Figure 14).

Case B

For an angle-of-attack of 44 degrees, since we were unable to obtain an inviscid solution at such a high angle-of-attack, the shock shape from the 25 degree inviscid solution was rotated to 44 degrees in a body-fixed coordinate system and used as input. This procedure caused some oscillations in the flowfield. Inspite of these oscillations, the predictions are quite good. The advantage of this procedure is that it is possible to obtain viscous solutions for various angles-of-attack that are substantially higher than that for which an inviscid solution can be easily obtained.

The wall pressure in the windward symmetry plane compares well with an Euler solution[41] (Figure 15), which was available at the present time for only half the length of the vehicle. Wall pressure predictions in other planes around the orbiter from the viscous shock-layer and Euler solutions[41] are also in good agreement (Figure 16).

In the windward symmetry plane the heat-transfer predictions from the viscous shock-layer compare well with the

AEDC[28] data (Figure 17). In other planes around the orbiter too, the heat-transfer rate shows higher values at the wing leading edge (Figure 18).

The u-velocity (Figure 19), pressure (Figure 20) and enthalpy (Figure 21) profiles normal to the body in the windward plane show trends similar to those for Case A.

Case C

The inviscid flowfield code STEIN[31] uses different curve-fits for the thermodynamic properties than those used in the VSL code. Different curve-fits of these data is probably the reason why the wall pressure predictions from the inviscid code are quite different from the viscous shock-layer values in the windward symmetry plane (Figure 22), while they are in quite good agreement for some other planes around the body (Figure 23).

No experimental data were available to compare the heat-transfer rate predictions for this case. The viscous shock-layer results for the windward (Figure 24) and other planes around the body indicate that the peaking at the wingtip noted in the previous cases is not as pronounced.

In the windward plane, the u-velocity (Figure 25), pressure (Figure 26) and enthalpy (Figure 27) profiles normal to the body showed slight jumps that might be caused by the

Prandtl number variation with temperature, which changes quite rapidly near the body.

Execution Times

The grid in the normal direction consisted of 101 unevenly spaced points in geometric progression so as to obtain better resolution at the wall where the gradients are large. Around the body the computational planes were evenly spaced, each 10 degrees apart (Figure 3). This procedure resulted in fairly large steps near the wingtip. A nonconstant distribution is needed to obtain better resolution in regions of large transverse curvatures such as near the wingtips. To keep computational costs down and because of the fairly large circumferential grid size, a maximum streamwise step size of S/Rn = 0.5 was used. Near the wingtip, where rapid changes are present, such a large step size is not desirable. The execution times (Table 1) for flowfield solutions on the windward surface, with some planes dropped on the leeward side, are relatively small compared to other time-dependent methods available. It must be noted that it takes approximately two hours of CDC 7600 time for a sphere nose when using the time dependent method developed by Kutler.[42]

For the equilirium air model, Thareja, Szema and Lewis[23] found that by using Bade curve-fits substantial reduction in

execution time was obtained when compared to the table look-up results without much loss of accuracy. Because of the large computing times involved in these cases, the Bade curve-fits were used for the equilibrium case.

Because of the good agreement for the predictions using an inviscid shock shape for $\alpha$ = 25 degrees, after rotation in a body-fixed coordinate system to $\alpha$ = 44 degrees as an initial guess of the shock shape at $\alpha$ = 44 degrees, it is shown that predictions can be made (i) at large angles-of-attack where it may be difficult to obtain inviscid solutions, and (ii) through an angle-of-attack range to simulate various lifting body orientations during a typical reentry flight trajectory for perfect gas and equilibrium air conditions for laminar flows. Since the major objective of this study is to predict the hypersonic flowfield over the windward surface of a lifting reentry vehicle such as the space shuttle, this method has been shown to yield good predictions of wall pressure and heat-transfer rates in reasonable computing times (about 35 minutes) on a general purpose computer (IBM 370/3032). The viscous shock-layer method has been shown to produce results of engineering accuracy and can be successfully used for a variety of potential applications.

# Chapter IV

## CONCLUSIONS AND RECOMMENDATIONS

The main objective of this study is to investigate the influence of noncircular bodies on the viscous shock-layer flow phenomena within reasonable computing times. A general nonorthogonal shock-layer analysis is used. Even with a relatively large grid, the present viscous shock-layer surface pressure, shock standoff distance and convective heat-transfer rate predictions are in good agreement with inviscid solutions and existing experimental data. The viscous shock-layer technique (VSL81) requires much less computing time than the time-dependent method. It should also be noted that the present VSL81 method can be used to predict the flowfield and heat-transfer distribution over the windward side only of a shuttle-like vehicle (not computing the lee-side flowfield) and thus it is possible to compute many flowfields with VSL81, which cannot presently be computed with any known PNS solution technique. For equilibrium air, curve-fits can be used with computing times that are comparable to the perfect gas model without much loss in accuracy.

Further development is necessary to have a nonconstant distribution of $\phi$ planes around the body. For better predictions, a finer grid size is also recommended.

## REFERENCES


1. Davis, R.T.: "Numerical Solution of the Hypersonic Viscous Shock-Layer Equations," AIAA J., May 1970, pp. 843-851.
2. Whitehead, R.E. and Davis, R.T.: "Numerical Solution to the Viscous Shock-Layer Blunt Body Problem with Inert Gas Injection," Sandia Laboratories, SC-CR-70-6162, January 1971.
3. Miner, E.W. and Lewis, C.H.: "Hypersonic Ionizing Air Viscous Shock-Layer Flows over Nonanalytic Blunt Bodies," NASA CR-2550, May 1975.
4. Miner E.W. and Lewis, C.H.: "Computer User's Guide for a Chemically Reacting Viscous Shock-Layer Program," NASA CR-2551, May 1975.
5. Miner, E.W. and Lewis, C.H.: "Viscous Shock-Layer Flows for the Space Shuttle Windward Plane of Symmetry," AIAA Paper No. 74-756, July 1974, also AIAA J., January 1976, pp. 64-69.
6. Murray, A.L., Waskiewicz, J.D. and Lewis, C.H.: "Laminar Viscous Shock-Layer Flows at Angle of Attack on the Shuttle Windward Streamline," AIAA Paper No. 77-87, January 1977.

7. Anderson, E.C. and Moss, J.N.: "Numerical Solution of the Hypersonic Viscous Shock-Layer Equations for Laminar, Transitional and Turbulent Flows of a Perfect Gas over Blunt Axially Symmetric Bodies," NASA TN D-7865, February 1975.

8. Eaton, R.R. and Larson, D.E.: "Laminar and Turbulent Viscous Shock-Layer Flow in Symmetry Planes of Bodies at Angles of Attack," AIAA Paper No. 74-599, June 1974.

9. Eaton, R.R. and Kaestner, P.C.: "Viscous Shock-Layer Flow in the Windward Plane of Cones at Angle of Attack," Sandia Laboratories, SC-RR-72-0449, March 1973.

10. Srivastava, B.N., Werle, M.J. and Davis, R.T.: "Stagnation Region Solutions of the Full Viscous Shock-Layer Equations," AIAA J., February 1976, pp.274-276.

11. Waskiewicz, J.D. and Lewis, C.H.: "Hypersonic Viscous Flows Over Sphere-Cones at High Angles of Attack," AIAA Paper No. 78-64, January 1978.

12. Waskiewicz, J.D., Murray, A.L. and Lewis, C.H.: "Hypersonic Viscous Shock-Layer Flow Over a Highly Cooled Sphere," AIAA J., February 1978, pp. 189-192.

13. Murray, A.L. and Lewis, C.H.: "Viscous Shock-Layer Flows Over Bodies During Reentry," AIAA Paper No. 78-259, January 1978.

14. Murray, A.L. and Lewis, C.H.: "Hypersonic Three-Dimensional Viscous Shock-Layer Flows Over Blunt Bodies," AIAA J., December 1978, pp. 1279-1286.

15. Murray, A.L. and Lewis, C.H.: "Three-Dimensional Fully Viscous Shock-Layer Flows Over Sphere-Cones at High Altitudes and High Angles of Attack," VPI&SU AERO-078, January 1978.

16. Murray, A.L. and Lewis, C.H.: "Heat and Mass-Transfer Effects on Three-Dimensional Viscous Shock-Layer Flows," AIAA Paper No. 78-844, May 1978.

17. Gogineni, P.R., Murray, A.L. and Lewis, C.H.: "Viscous Flows Over Slender Spherically Blunted Cones at Large Angles of Attack Including Mass-Transfer and Low Reynolds Number Effects," AIAA Paper No. 78-1188, July 1978.

18. Tree, I.K., Melson, N.D. and Lewis, C.H.: "Low Reynolds Number Hypersonic Ionizing Viscous Shock-Layer Flows Over the Jovian Probe," AIAA Paper No. 79-1080, June 1979.

19. Gogineni, P.R. and Lewis, C.H.: "Three-Dimensional Viscous Hypersonic Flows Over General Bodies," AIAA Paper No. 80-0029, January 1980.

20. Szema, K.Y. and Lewis, C.H.: "Three-Dimensional Hypersonic Laminar, Transitional and/or Turbulent

Shock-Layer Flows," AIAA Paper No. 80-1457, July 1980.

21. Cebeci, T.: "Behavior of Turbulent Flows near a Porous Wall with Pressure Gradient," AIAA J., December 1970, pp. 2152-2156.

22. Dhawan, S. and Narasimha, R.: "Some Properties of Boundary Layer Flow During the Transition from Laminar to Turbulent Motion," Journal of Fluid Mechanics, Vol. 3, Pt. 4, January 1958, pp. 418-436.

23. Thareja, R.R., Szema, K.Y. and Lewis, C.H.: "Effects of Chemical Equilibrium on Three-Dimensional Viscous Shock-Layer Analysis of Hypersonic Laminar or Turbulent Flows," AIAA Paper No. 82-0305, January 1982.

24. Szema, K.Y. and Lewis, C.H.: "Computation of Three-Dimensional Viscous Flow Over Blunt Lifting Bodies at High Angle of Attack," 12th Navy Symposium on Aeroballistics, DTNSRDC, Maryland, May 1981.

25. Szema, K.Y. and Lewis, C.H.: "Three-Dimensional Viscous Shock-Layer Flows Over Lifting Bodies at High Angles of Attack," AIAA Paper No. 81-1146, June 1981.

26. Carter, L.D. and Martindale, W.R.: "Test Results from the NASA/Rockwell International Space Shuttle Test (0H9) Conducted in the AEDC-vKF Tunnel B," AEDC-DR-74-9, January 1974.

27. Martindale, W.R.: "Test Results from the NASA/Rockwell International Space Shuttle Test (OH4B) Conducted in the AEDC-vKF Tunnel B," AEDC-DR-74-8, January 1974.

28. Herrera, B.J.: "Results from a Convective Heat Transfer Rate Distribution Test on a 0.0175 Scale Model (22-0) of the Rockwell International Vehicle 4 Space Shuttle Configuration in the AEDC-vKF Tunnel B," NASA-CR-147626, 1976.

29. Vachris, A. F. and Yaeger, L.S.: "QUICK-GEOMETRY: A Rapid Response Method for Mathematically Modeling Configuration Geometry," NASA SP-390, 1975, pp.49-73.

30. Moretti, G. and Bleich, G.: "Three-Dimensional Flow Around Blunt Bodies," AIAA J., Vol. 5, 1967.

31. Marconi, F. and Yaeger, L.: "Development of a Computer Code for Calculating the Steady Super/Hypersonic Inviscid Flow around Real Configurations," NASA CR-2675, April 1976.

32. Miner, E.W., Anderson, E.C., Lewis C.H.: "A Computer Program for Two-Dimensional and Axisymmetric Nonreacting Perfect Gas and Equilibrium Chemically Reacting Laminar, Transitional and/or Turbulent Boundary Layer Flows," VPI-E-71-8, May 1971.

33. Lordi, J.A., Mates, R.E. and Moselle, J.R.: "A Computer Program for the Numerical Solution of Nonequilibrium Expansions of Reacting Gas Mixtures," CAL RPT No. AD-K89-A-6, 1965.

34. Hansen, C.F.: "Approximations for the Thermodynamic and Transport Properties of High-Temperature Air," NASA TR R-50, 1959.

35. Cohen, N.B.: "Correlation Formulas and Tables of Density and Some Thermodynamic Properties of Equilibrium Dissociating Air for Use in Solutions of the Boundary-Layer Equations," NASA TN D-194, February 1960.

36. Moeckel, W.E. and Weston, K.C.: "Composition and Thermodynamic Properties of Air in Chemical Equilibrium," NACA TN 4265, 1958.

37. Bade W.L.: "Simple Analytical Approximation to the Equation of State of Dissociated Air," ARS Journal, Vol 29, No. 4, April 1959.

38. Blottner, F.G.: "Finite Difference Method of Solution of Boundary-Layer Equation," AIAA J., February 1970, pp. 193-205.

39. Helliwell, W.S., Dickinson, R.P. and Lubard, S.C.: "Viscous Flow Over Arbitrary Geometries at High Angles of Attack," AIAA Paper No. 80-0064, January 1980.

40. Frieders, M.C. and Lewis, C.H.: "Effects of Mass Transfer into Laminar and Turbulent Boundary Layers over Cones at Angle of Attack," VPI-AERO-031, March 1975.

41. Hamilton, H.H.: private communication.

42. Kutler, P., Pedelty, J.A. and Pulliam, T.H.: "Supersonic Flow over Three Dimensional Ablated Nosetips Using an Unsteady Implicit Numerical Procedure," AIAA Paper No. 80-0063, January 1980.

43. Aris, R.: Vectors, Tensors, and the Basic Equations of Fluid Mechanics, Prentice-Hall Inc., 1962.

## Appendix A

## VISCOUS SHOCK-LAYER EQUATIONS

The basic equations are derived from the steady Navier-Stokes equations in general body-oriented tensor form. The coordinate system requires orthogonality only at the body surface. The normal velocoity v and normal coordinate are assumed to be of order $\epsilon$, and all terms which are of higher order than $\epsilon$ are neglected. For these equations and general tensor theory, Reference 43 can be useful.

Momentum Equations:

We have

$$\rho a^i + g^{ij} P_{,j} = \rho f^i + \tau^{ij}{}_{,j} \tag{A1}$$

Assuming steady flow and no body forces, after non-dimensionalizing A1, we have:

$$\frac{\rho_\infty^* U_\infty^{*2}}{R_n^*}\left[\rho a^i + g^{ij} P_{,j}\right] = \frac{\mu_{ref}^* U_\infty^*}{R_n^{*2}} \tau^{ij}{}_{,j}$$

Denoting

$$\epsilon^2 = \frac{\mu_{ref}^*}{\rho_\infty^* U_\infty^* R_n^*}$$

we have

$$\rho a^i + g^{ij} P_{,j} = \epsilon^2 \tau^{ij}{}_{,j} \tag{A2}$$

In A2, the $a^i$ can be written as

$$a^i = \frac{\partial V^i}{\partial x^j} V^j + \left\{ \begin{matrix} i \\ j\ k \end{matrix} \right\} V^j V^k \,, \quad i = 1, 2, 3$$

from which we get

$$a^1 = u\frac{\partial u}{\partial \xi_1} + v\frac{\partial u}{\partial \xi_2} + w\frac{\partial u}{\partial \xi_3} + u^2 \left\{ \begin{matrix} 1 \\ 1\ 1 \end{matrix} \right\} + 2uv \left\{ \begin{matrix} 1 \\ 1\ 2 \end{matrix} \right\}$$
$$+ 2uw \left\{ \begin{matrix} 1 \\ 1\ 3 \end{matrix} \right\} + v^2 \left\{ \begin{matrix} 1 \\ 2\ 2 \end{matrix} \right\} + 2vw \left\{ \begin{matrix} 1 \\ 2\ 3 \end{matrix} \right\} + w^2 \left\{ \begin{matrix} 1 \\ 3\ 3 \end{matrix} \right\}$$

$$a^2 = u\frac{\partial v}{\partial \xi_1} + v\frac{\partial v}{\partial \xi_2} + w\frac{\partial v}{\partial \xi_3} + u^2 \left\{ \begin{matrix} 2 \\ 1\ 1 \end{matrix} \right\} + 2uv \left\{ \begin{matrix} 2 \\ 1\ 2 \end{matrix} \right\} \qquad \text{(A3)}$$
$$+ 2uw \left\{ \begin{matrix} 2 \\ 1\ 3 \end{matrix} \right\} + v^2 \left\{ \begin{matrix} 2 \\ 2\ 2 \end{matrix} \right\} + 2vw \left\{ \begin{matrix} 2 \\ 2\ 3 \end{matrix} \right\} + w^2 \left\{ \begin{matrix} 2 \\ 3\ 3 \end{matrix} \right\}$$

$$a^3 = u\frac{\partial w}{\partial \xi_1} + v\frac{\partial w}{\partial \xi_2} + w\frac{\partial w}{\partial \xi_3} + u^2 \left\{ \begin{matrix} 3 \\ 1\ 1 \end{matrix} \right\} + 2uv \left\{ \begin{matrix} 3 \\ 1\ 2 \end{matrix} \right\}$$
$$+ 2uw \left\{ \begin{matrix} 3 \\ 1\ 3 \end{matrix} \right\} + v^2 \left\{ \begin{matrix} 3 \\ 2\ 2 \end{matrix} \right\} + 2vw \left\{ \begin{matrix} 3 \\ 2\ 3 \end{matrix} \right\} + w^2 \left\{ \begin{matrix} 3 \\ 3\ 3 \end{matrix} \right\}$$

For the stress terms,

$$\tau^{ij} = \lambda V^k{}_{,k}\, g^{ij} + 2\mu e^{ij} \qquad \text{(A4)}$$

where

$$e^{ij} = g^{mi} g^{jn} e_{mn}, \qquad \text{and} \qquad \text{(A5)}$$

$$e_{mn} = \frac{1}{2}\left( V_{m,n} + V_{n,m} \right) \text{ with} \qquad \text{(A6)}$$

$$V_m = g_{mk} V^k$$

Note that $g_{12} = g_{21} = 0$, and
$g_{23} = g_{32} = 0$, and

$$g^{11} = \frac{g_{22} g_{33}}{g} \qquad g^{12} = 0 \qquad g^{13} = \frac{-g_{22} g_{13}}{g}$$

$$g^{21} = 0 \qquad g^{22} = \frac{1}{g_{22}} \qquad g^{23} = 0 \qquad \text{(A7)}$$

$$g^{31} = \frac{-g_{22} g_{13}}{g} \qquad g^{32} = 0 \qquad g^{33} = \frac{g_{11} g_{22}}{g}$$

with

$$g = g_{11} g_{22} g_{33} - g_{22} g_{13}^2$$

From A6, we have

$$e_{mn} = \frac{1}{2}\left[ g_{mk} \frac{\partial v^k}{\partial x^n} + g_{nk} \frac{\partial v^k}{\partial x^m} \right] \qquad \text{(A8)}$$

Retaining terms of order at least $(1/\epsilon)$, we get

$$e_{11} = 0$$

$$e_{12} = \frac{1}{2}\left[ g_{11} \frac{\partial u}{\partial \xi_2} + g_{13} \frac{\partial w}{\partial \xi_2} \right]$$

$$e_{13} = \frac{1}{2}\left[ g_{11} \frac{\partial u}{\partial \xi_3} + g_{13} \frac{\partial w}{\partial \xi_3} \right]$$

$$e_{21} = e_{12}$$

$$e_{22} = g_{21} \frac{\partial u}{\partial \xi_2} + g_{22} \frac{\partial v}{\partial \xi_2} \qquad \text{(A9)}$$

$$e_{23} = \frac{1}{2}\left[ g_{22} \frac{\partial v}{\partial \xi_3} + g_{31} \frac{\partial u}{\partial \xi_2} + g_{33} \frac{\partial w}{\partial \xi_2} \right]$$

$$e_{31} = e_{13}$$

$$e_{32} = e_{23}$$

$$e_{33} = g_{31} \frac{\partial u}{\partial \xi_3} + g_{33} \frac{\partial w}{\partial \xi_3}$$

From A5, A6, A7 and A9, we get

$$e^{11} = -\frac{g_{22} g_{13}}{g} \frac{\partial u}{\partial \xi_3}$$

$$e^{12} = \frac{1}{2 g_{22}} \frac{\partial u}{\partial \xi_2} - \frac{g_{22} g_{13}}{2g} \frac{\partial v}{\partial \xi_2}$$

$$e^{13} = \frac{g_{11} g_{22}}{2g} \frac{\partial u}{\partial \xi_3} - \frac{g_{22} g_{13}}{2g} \frac{\partial w}{\partial \xi_3}$$

$$e^{21} = e^{12}$$

$$e^{22} = \frac{1}{g_{22}} \frac{\partial v}{\partial \xi_2} \qquad \text{(A10)}$$

$$e^{23} = \frac{1}{2 g_{22}} \frac{\partial w}{\partial \xi_2} + \frac{g_{11} g_{22}}{2g} \frac{\partial v}{\partial \xi_3}$$

$$e^{31} = e^{13}$$

$$e^{32} = e^{23}$$

$$e^{33} = \frac{g_{11} g_{22}}{g} \frac{\partial w}{\partial \xi_3}$$

Also,

$$V^k_{;k} = \frac{1}{\sqrt{g}} \frac{\partial}{\partial x^k}(\sqrt{g}\, V^k)$$

$$= \frac{1}{\sqrt{g}}\left[\frac{\partial}{\partial \xi_1}(\sqrt{g}\,u) + \frac{\partial}{\partial \xi_2}(\sqrt{g}\,v) + \frac{\partial}{\partial \xi_3}(\sqrt{g}\,w)\right]$$

$$= \frac{\partial v}{\partial \xi_2} + \frac{\partial w}{\partial \xi_3} \qquad \text{(A11)}$$

Assuming Stokes' Hypothesis (i.e., $\lambda - \frac{2}{3}\mu = 0$), and from A4, A7, A10 and A11, we get

$$\tau^{11} = \mu\left[-\frac{2}{3}\frac{g_{22}g_{33}}{g}\frac{\partial v}{\partial \xi_2} - \frac{2}{3}\frac{g_{22}g_{33}}{g}\frac{\partial w}{\partial \xi_3} - 2\frac{g_{22}g_{13}}{g}\frac{\partial u}{\partial \xi_3}\right]$$

$$\tau^{12} = \mu\left[\frac{1}{g_{22}}\frac{\partial u}{\partial \xi_2} - \frac{g_{22}g_{13}}{g}\frac{\partial v}{\partial \xi_3}\right]$$

$$\tau^{13} = \mu\left[-\frac{1}{3}\frac{g_{22}g_{13}}{g}\frac{\partial w}{\partial \xi_3} + \frac{2}{3}\frac{g_{22}g_{13}}{g}\frac{\partial v}{\partial \xi_2} + \frac{g_{11}g_{22}}{g}\frac{\partial u}{\partial \xi_3}\right] \qquad \text{(A12)}$$

$$\tau^{21} = \tau^{12}$$

$$\tau^{22} = \mu\left[\frac{4}{3}\frac{1}{g_{22}}\frac{\partial v}{\partial \xi_2} - \frac{2}{3}\frac{1}{g_{22}}\frac{\partial w}{\partial \xi_3}\right]$$

$$\tau^{23} = \mu\left[\frac{1}{g_{22}}\frac{\partial w}{\partial \xi_2} + \frac{g_{11}g_{22}}{g}\frac{\partial v}{\partial \xi_3}\right]$$

$$\tau^{31} = \tau^{13}$$

$$\tau^{32} = \tau^{23}$$

$$\tau^{33} = \mu\left[\frac{4}{3}\frac{g_{11}g_{22}}{g}\frac{\partial w}{\partial \xi_3} - \frac{2}{3}\frac{g_{11}g_{22}}{g}\frac{\partial v}{\partial \xi_2}\right]$$

Now,

$$\tau^{ij}{}_{;j} = \frac{1}{\sqrt{g}}\frac{\partial}{\partial x^j}\left(\sqrt{g}\,\tau^{ij}\right) + \tau^{jk}\left\{\begin{matrix} i \\ j\ k \end{matrix}\right\} \qquad \text{(A13)}$$

The right hand side of A2 contains all the viscous effects. Keeping only terms that are of order and dropping all terms that make the equations elliptic in the streamwise and crossflow directions, we get from A2, A3, A12, and A13:

$\xi_1$-Momentum Equation:

$$\rho u\frac{\partial u}{\partial \xi_1} + \rho v\frac{\partial u}{\partial \xi_2} + \rho w\frac{\partial u}{\partial \xi_3} + \rho\left[u^2\left\{\begin{matrix} 1 \\ 1\ 1 \end{matrix}\right\} + 2uv\left\{\begin{matrix} 1 \\ 1\ 2 \end{matrix}\right\}\right.$$

$$\left. + 2uw\left\{\begin{matrix} 1 \\ 1\ 3 \end{matrix}\right\} + v^2\left\{\begin{matrix} 1 \\ 2\ 2 \end{matrix}\right\} + 2vw\left\{\begin{matrix} 1 \\ 2\ 3 \end{matrix}\right\} + w^2\left\{\begin{matrix} 1 \\ 3\ 3 \end{matrix}\right\}\right]$$

$$+ \frac{g_{22}}{g}\left[g_{33}\frac{\partial p}{\partial \xi_1} - g_{13}\frac{\partial p}{\partial \xi_3}\right]$$

$$= \frac{\epsilon^2}{g_{22}}\left[\frac{\partial \mu}{\partial \xi_2}\frac{\partial u}{\partial \xi_2} + \mu\frac{\partial^2 u}{\partial \xi_2^2}\right]$$

(A14)

$\xi_2$ -Momentum Equation:

$$\rho u \frac{\partial v}{\partial \xi_1} + \rho v \frac{\partial v}{\partial \xi_2} + \rho w \frac{\partial v}{\partial \xi_3} + \rho \left[ u^2 \left\{ \begin{matrix} 2 \\ 1 \ 1 \end{matrix} \right\} + 2uv \left\{ \begin{matrix} 2 \\ 1 \ 2 \end{matrix} \right\} + 2uw \left\{ \begin{matrix} 2 \\ 1 \ 3 \end{matrix} \right\} + v^2 \left\{ \begin{matrix} 2 \\ 2 \ 2 \end{matrix} \right\} + 2vw \left\{ \begin{matrix} 2 \\ 2 \ 3 \end{matrix} \right\} + w^2 \left\{ \begin{matrix} 2 \\ 3 \ 3 \end{matrix} \right\} \right]$$

$$+ \frac{1}{g_{22}} \frac{\partial p}{\partial \xi_2} = 0$$

(A15)

$\xi_3$ -Momentum Equation:

$$\rho u \frac{\partial w}{\partial \xi_1} + \rho v \frac{\partial w}{\partial \xi_2} + \rho w \frac{\partial w}{\partial \xi_3} + \rho \left[ u^2 \left\{ \begin{matrix} 3 \\ 1 \ 1 \end{matrix} \right\} + 2uv \left\{ \begin{matrix} 3 \\ 1 \ 2 \end{matrix} \right\} + 2uw \left\{ \begin{matrix} 3 \\ 1 \ 3 \end{matrix} \right\} + v^2 \left\{ \begin{matrix} 3 \\ 2 \ 2 \end{matrix} \right\} + 2vw \left\{ \begin{matrix} 3 \\ 2 \ 3 \end{matrix} \right\} + w^2 \left\{ \begin{matrix} 3 \\ 3 \ 3 \end{matrix} \right\} \right]$$

$$+ \frac{g_{22}}{g} \left[ g_{11} \frac{\partial p}{\partial \xi_3} - g_{13} \frac{\partial p}{\partial \xi_1} \right]$$

$$= \frac{\epsilon^2}{g_{22}} \left[ \frac{\partial \mu}{\partial \xi_2} \frac{\partial w}{\partial \xi_2} + \mu \frac{\partial^2 w}{\partial \xi_2^2} \right]$$

(A16)

Energy Equation:

$$\rho \frac{Dh}{Dt} - \frac{DP}{Dt} = -\operatorname{div} q + \Phi \tag{A17}$$

Since $\frac{DA}{Dt} = \frac{\partial A}{\partial t} + V^i A,i$ we have

$$\rho V^i h,i - V^i P,i = -\operatorname{div} q + \Phi \tag{A18}$$

Nondimensionalizing, we get:

$$\frac{\rho_\infty^* U_\infty^{*3}}{R_n^*}\left[\rho V^i h,i - V^i P,i\right] = \frac{\mu_{ref}^* U_\infty^{*2}}{R_n^{*2}}\left[-\operatorname{div} q + \Phi\right]$$

$$\text{or, } \rho V^i h,i - V^i P,i = \epsilon^2\left[-\operatorname{div} q + \Phi\right] \tag{A19}$$

Also,

$$\begin{aligned}\Phi &= \bar{\bar{\tau}}\ \text{grad}\ \vec{V} \\ &= \tau^{ij} Vi,j \\ &= \tau^{ij} e_{ij}\end{aligned} \tag{A20}$$

From A9, A12 and A20, we get:

$$\begin{aligned}\Phi/\mu = {} & \frac{q_{11}}{q_{22}}\left(\frac{\partial u}{\partial \xi_2}\right)^2 + 2\frac{q_{31}}{q_{22}}\frac{\partial u}{\partial \xi_2}\frac{\partial w}{\partial \xi_2} + \frac{q_{33}}{q_{22}}\left(\frac{\partial w}{\partial \xi_2}\right)^2 \\ & + \left[\frac{q_{11}^2 q_{22}}{q}\left(\frac{\partial u}{\partial \xi_3}\right)^2 + 2\frac{q_{11} q_{22} q_{33}}{q}\frac{\partial u}{\partial \xi_3}\frac{\partial w}{\partial \xi_3}\right. \\ & + \left.\frac{4}{3}\left(\frac{\partial v}{\partial \xi_2}\right)^2 - \frac{4}{3}\frac{\partial w}{\partial \xi_2}\frac{\partial w}{\partial \xi_3} + 2\frac{\partial v}{\partial \xi_3}\frac{\partial w}{\partial \xi_2}\right.\end{aligned}$$

$$+ \frac{g_{11} g_{22}^2}{g} \left(\frac{\partial v}{\partial \xi_3}\right)^2 + \left(\frac{1}{3} + \frac{g_{11} g_{22} g_{33}}{g}\right)\left(\frac{\partial w}{\partial \xi_3}\right)^2\Bigg]$$

The terms in square brackets are of higher order than and are therefore neglected.

$$\frac{\Phi}{\mu} = \frac{g_{11}}{g_{22}}\left(\frac{\partial u}{\partial \xi_2}\right)^2 + 2\frac{g_{31}}{g_{22}}\frac{\partial u}{\partial \xi_2}\frac{\partial w}{\partial \xi_2} + \frac{g_{33}}{g_{22}}\left(\frac{\partial w}{\partial \xi_2}\right)^2 \qquad \text{(A21)}$$

$$\begin{aligned} -\operatorname{div} q &= -\operatorname{div}\left[-k/C_p \operatorname{grad} h\right] \\ &= \operatorname{div}\left[\mu/Pr \operatorname{grad} h\right] \\ &= \operatorname{div}\left[\mu/Pr \frac{\partial h}{\partial \xi_2}\right] \\ &= \frac{1}{g_{22}}\left[\frac{\partial}{\partial \xi_2}\left(\frac{\mu}{Pr}\right)\frac{\partial h}{\partial \xi_2} + \frac{\mu}{Pr}\frac{\partial^2 h}{\partial \xi_2^2}\right] \end{aligned} \qquad \text{(A22)}$$

From A19, A21 and A22, we get:

$$\rho u \frac{\partial h}{\partial \xi_1} + \rho v \frac{\partial h}{\partial \xi_2} + \rho w \frac{\partial h}{\partial \xi_3} - \left[u \frac{\partial p}{\partial \xi_1} + v \frac{\partial p}{\partial \xi_2} + w \frac{\partial p}{\partial \xi_3}\right]$$

$$= \frac{\epsilon^2}{g_{22}}\left[\frac{\partial}{\partial \xi_2}\left(\frac{\mu}{Pr}\right)\frac{\partial h}{\partial \xi_2} + \frac{\mu}{Pr}\frac{\partial^2 h}{\partial \xi_2^2}\right]$$

$$+ \frac{\epsilon^2 \mu}{g_{22}}\left[g_{11}\left(\frac{\partial u}{\partial \xi_2}\right)^2 + 2 g_{13}\frac{\partial u}{\partial \xi_2}\frac{\partial w}{\partial \xi_2}\right.$$

$$\left. + g_{33}\left(\frac{\partial w}{\partial \xi_2}\right)^2\right]$$

(A23)

Continuity Equation:

For steady flow,

$$\operatorname{div}(\rho \vec{v}) = 0$$

$$\frac{\partial}{\partial \xi_1}(\rho u g^{1/2}) + \frac{\partial}{\partial \xi_2}(\rho v g^{1/2}) + \frac{\partial}{\partial \xi_3}(\rho w g^{1/2}) = 0$$

(A24)

Equation of State:

$$\rho = \rho(p,h)$$

(A25)

Prandtl Number:

$$Pr = Pr(p,h)$$

(A26)

## Appendix B

## CURVILINEAR COORDINATES AND GRID GENERATION

This appendix gives a brief description of curvilinear coordinates in three dimensions related to the development of the main computer code. Of particular importance are the metric functions, since these define the length of and angle between the coordinate lines.

In a body-oriented cylindrical coordinate system $(z,r,\phi)$, we use the notation; $\zeta_1 = z$, $\zeta_2 = r$, $\zeta_3 = \phi$ and corresponding vectors $\vec{\gamma}_1$, $\vec{\gamma}_2$, $\vec{\gamma}_3$, and $|\vec{\gamma}_1| = 1$, $|\vec{\gamma}_2| = 1$, $|\vec{\gamma}_3| = r$.

Now define general curvilinear coordinates from the cylindrical coordinates. Let $\xi_1$, $\xi_2$, $\xi_3$ be the three independent directions with direction vectors $\vec{g}_1$, $\vec{g}_2$, $\vec{g}_3$. Then

$$\vec{g}_k = \frac{\partial \zeta_m}{\partial \xi_k} \vec{\gamma}_m \tag{B1}$$

Now

$$\begin{aligned} ds^2 &= ( d\xi_1 \vec{g}_1 + d\xi_2 \vec{g}_2 + d\xi_3 \vec{g}_3 )^2 \\ &= g_{11} d\xi_1 d\xi_1 + g_{12} d\xi_1 d\xi_2 + g_{13} d\xi_1 d\xi_3 \\ &\quad + g_{21} d\xi_2 d\xi_1 + g_{22} d\xi_2 d\xi_2 + g_{23} d\xi_2 d\xi_3 \\ &\quad + g_{31} d\xi_3 d\xi_1 + g_{32} d\xi_3 d\xi_2 + g_{33} d\xi_3 d\xi_3 \end{aligned} \tag{B2}$$

where

$$g_{ij} = \vec{g}_i \cdot \vec{g}_j = \frac{\partial z}{\partial \xi_i} \frac{\partial z}{\partial \xi_j} + \frac{\partial r}{\partial \xi_i} \frac{\partial r}{\partial \xi_j} + r^2 \frac{\partial \phi}{\partial \xi_i} \frac{\partial \phi}{\partial \xi_j} \tag{B3}$$

It is noted that $g_{ij} = g_{ji}$ for $i,j = 1,2,3$ (symmetric property), and the metric is expressed as a function of the curvilinear coordinate, i.e., $g_{ij} = g_{ij}(\xi_1, \xi_2, \xi_3)$.

If $g_{ij} = 0$ for $i \neq j$ everywhere, then the coordinate system is orthogonal, but in general it will be non-orthogonal. Also in general, the $\vec{g}_i$ vectors are not unit vectors.

In addition to the $\vec{g}_1, \vec{g}_2, \vec{g}_3$ vectors, it is useful to have vectors perpendicular to these, i.e.

$$\vec{g}^i \cdot \vec{g}_j = \delta^i_j \tag{B4}$$

To construct these vectors, $\vec{g}^i$ can be written as

$$\vec{g}^i = \sum_k g^{ik} \vec{g}_k \tag{B5}$$

since $\vec{g}_1, \vec{g}_2, \vec{g}_3$ form a basis. Then

$$\delta^i_j = \vec{g}^i \cdot \vec{g}_j = \sum_k g^{ik} \vec{g}_k \cdot \vec{g}_j = \sum_k g^{ik} g_{kj} \tag{B6}$$

or

$$\begin{bmatrix} g^{11} & g^{12} & g^{13} \\ g^{21} & g^{22} & g^{23} \\ g^{31} & g^{32} & g^{33} \end{bmatrix} \times \begin{bmatrix} g_{11} & g_{12} & g_{13} \\ g_{21} & g_{22} & g_{23} \\ g_{31} & g_{32} & g_{33} \end{bmatrix} = \begin{bmatrix} 1 & 0 & 0 \\ 0 & 1 & 0 \\ 0 & 0 & 1 \end{bmatrix} \tag{B7}$$

To find the $g^{ij}$ then simply invert the $(g_{km})$ matrix. In the present streamline coordinate system,

$$\begin{aligned} g^{11} &= \frac{g_{22} g_{33}}{g} \\ g^{13} &= \frac{-g_{22} g_{33}}{g} \\ g^{22} &= \frac{1}{g_{22}} \\ g^{33} &= \frac{g_{11}}{g} \end{aligned} \tag{B8}$$

where

$$g = g_{11} \; g_{22} \; g_{33} - g_{13} \; g_{22} \; g_{31} \tag{B9}$$

To derive the Navier-Stokes equations in curvilinear coordinates, we utilize

$$\frac{\partial}{\partial \xi_j} \vec{g}_k = \sum_i \left\{ {}^{i}_{j\,k} \right\} \vec{g}_i \tag{B10}$$

where

$$\left\{ {}^{i}_{j\,k} \right\} = \frac{1}{2} \sum_m g^{im} \left[ \frac{\partial g_{mk}}{\partial \xi_j} + \frac{\partial g_{mj}}{\partial \xi_k} - \frac{\partial g_{jk}}{\partial \xi_m} \right] \tag{B11}$$

and

$$\sum_i \left\{ {}^{i}_{m\,i} \right\} = \frac{1}{\sqrt{g}} \frac{\partial}{\partial \xi_m} \left( \sqrt{g} \right) \tag{B12}$$

These relations may be found in Reference 39.

In order to generate the non-orthogonal coordinates, we start at the body and calculate out to the shock. Since there is symmetry about the pitch plane, only one side of the body needs to be considered. The surface of the body is written in cylindrical coordinates in the form

$$r = r\,(z, \phi) \tag{B13}$$

On the body surface, constant $\xi_3$ lines are obtained from the intersection of a constant $\phi$ plane with the body, so that $\xi_3 = \phi$ . From the QUICK geometry definition, for a given s in a plane, the value of z and r for the body is known. In order to obtain the coordinates in the region from the body surface to the shock surface, we start by taking the cross product, $\vec{g}_3 \times \vec{g}_1$ . If $\vec{i}'$, $\vec{j}'$, $\vec{k}'$ are unit vectors in the cylindrical coordinates, then the coordinate vectors are given by:

$$\vec{g_m} = \frac{\partial z}{\partial \xi_m}\,\vec{i'} + \frac{\partial r}{\partial \xi_m}\,\vec{j'} + r\,\frac{\partial \phi}{\partial \xi_m}\,\vec{k'}, \qquad m=1,2,3 \tag{B14}$$

Defining $\vec{n}$ as the cross product between $\vec{g_3}$ and $\vec{g_1}$, we have

$$\vec{n} = n_1\vec{i'} + n_2\vec{j'} + n_3\vec{k'} \tag{B15}$$

where

$$\begin{aligned} n_1 &= r\left(\frac{\partial r}{\partial \xi_3}\frac{\partial \phi}{\partial \xi_1} - \frac{\partial \phi}{\partial \xi_3}\frac{\partial r}{\partial \xi_1}\right), \\ n_2 &= r\left(\frac{\partial z}{\partial \xi_1}\frac{\partial \phi}{\partial \xi_3} - \frac{\partial z}{\partial \xi_3}\frac{\partial \phi}{\partial \xi_1}\right), \\ n_3 &= \left(\frac{\partial z}{\partial \xi_3}\frac{\partial r}{\partial \xi_1} - \frac{\partial r}{\partial \xi_3}\frac{\partial z}{\partial \xi_1}\right), \end{aligned} \tag{B16}$$

Setting $\vec{g_2}/\sqrt{g_{22}} = \vec{n}/|\vec{n}|$, we obtain

$$\begin{aligned} \frac{\partial z}{\partial \xi_2} &= n_1\sqrt{g_{22}}\,/\,|\vec{n}|, \\ \frac{\partial r}{\partial \xi_2} &= n_2\sqrt{g_{22}}\,/\,|\vec{n}|, \\ \frac{\partial \phi}{\partial \xi_2} &= n_3\sqrt{g_{22}}\,/\,r\,|\vec{n}|, \end{aligned} \tag{B17}$$

Equations B17 are integrated from the body surface $\xi_2 = 0$ to the shock surface. With the coordinates constructed in this manner, $\vec{g_2}$ is always orthogonal to $\vec{g_3}$ and $\vec{g_1}$ (i.e., $g_{23} = g_{21} = 0$), but $\vec{g_1}$ is not necessarily orthogonal to $\vec{g_3}$. By setting $\sqrt{g_{22}} = 1$, the shock will correspond to $\xi_2 = 1$.

Once the coordinates of the computational mesh

$z(\xi_1, \xi_2, \xi_3)$, $r(\xi_1, \xi_2, \xi_3)$ and $\phi(\xi_1, \xi_2, \xi_3)$ are known everywhere, the metrics can be obtained by numerical differentiation:

$$g_{ij} = \frac{\partial z}{\partial \xi_i}\frac{\partial z}{\partial \xi_j} + \frac{\partial r}{\partial \xi_i}\frac{\partial r}{\partial \xi_j} + r\frac{\partial \phi}{\partial \xi_i}\frac{\partial \phi}{\partial \xi_j} \qquad i,j=1,2,3 \tag{B18}$$

From B18, we can compute the following important quantities used in the viscous shock-layer equations. These are the determinant of the metric, g, which for our system is:

$$g = g_{11}\, g_{22}\, g_{33} - g_{22}\, g_{13}^2 \tag{B19}$$

and the Christoffel symbols of the second kind:

$$\left\{ \begin{matrix} i \\ j\ k \end{matrix} \right\} = \frac{1}{2} \sum_m g^{im} \left[ \frac{\partial g_{mk}}{\partial \xi_j} + \frac{\partial g_{mj}}{\partial \xi_k} - \frac{\partial g_{jk}}{\partial \xi_m} \right] \tag{B20}$$

where the $g^{ij}$ are defined by

$$\sum_k g^{ik}\, g_{kj} = \delta_j^i \,. \tag{B21}$$

TABLE 1

Test Case Conditions

| | CASE A | CASE B | CASE C |
|---|---|---|---|
| Mach Number | 7.92 | 7.93 | 9.50 |
| $\alpha$ , deg | 25 | 44 | 25 |
| $T_\infty$ , R | 94.87 | 93.24 | 485.78 |
| $p_\infty$ , psia | 0.0119030 | 0.0226010 | 0.0115686 |
| $\rho_\infty$ , slug/ft | 1.0528E-5 | 2.0341E-5 | 1.9984E-6 |
| $T_w$ , R | 540 | 550 | 2000 |
| $Re_\infty$ , $ft^{-1}$ | 5.5697E5 | 1.9014E6 | 5.7752E4 |
| Gas Model | perfect gas | perfect gas | equilibrium air BADE |
| $\xi_1$ steps | 111 | 118 | 105 |
| Comp Time*, min | 31 | 31 | 37 |

* IBM 370/3032 with FORTHX opt(2) compiler

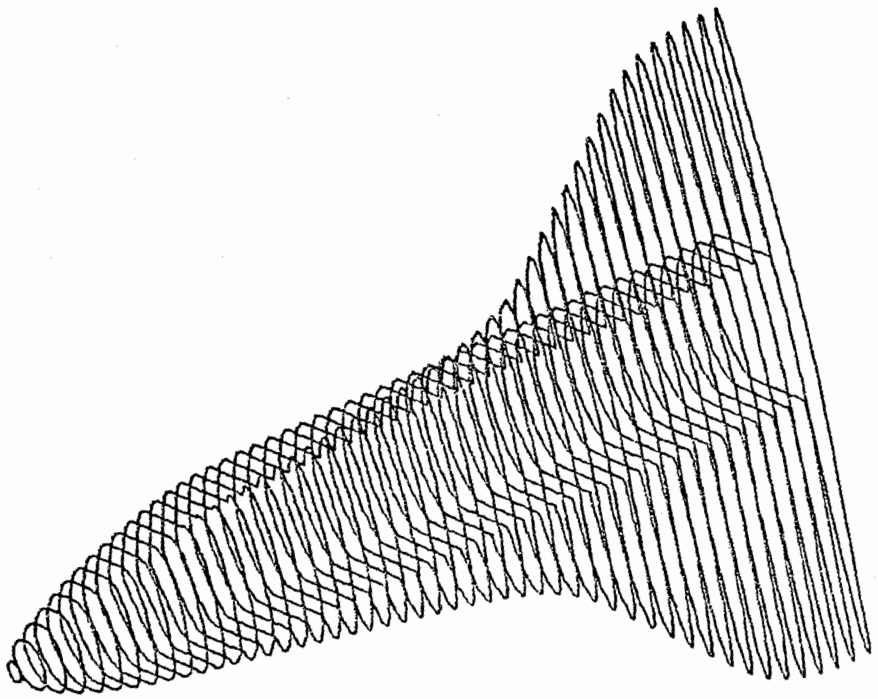

Figure 1: Shuttle orbiter geometry using QUICK

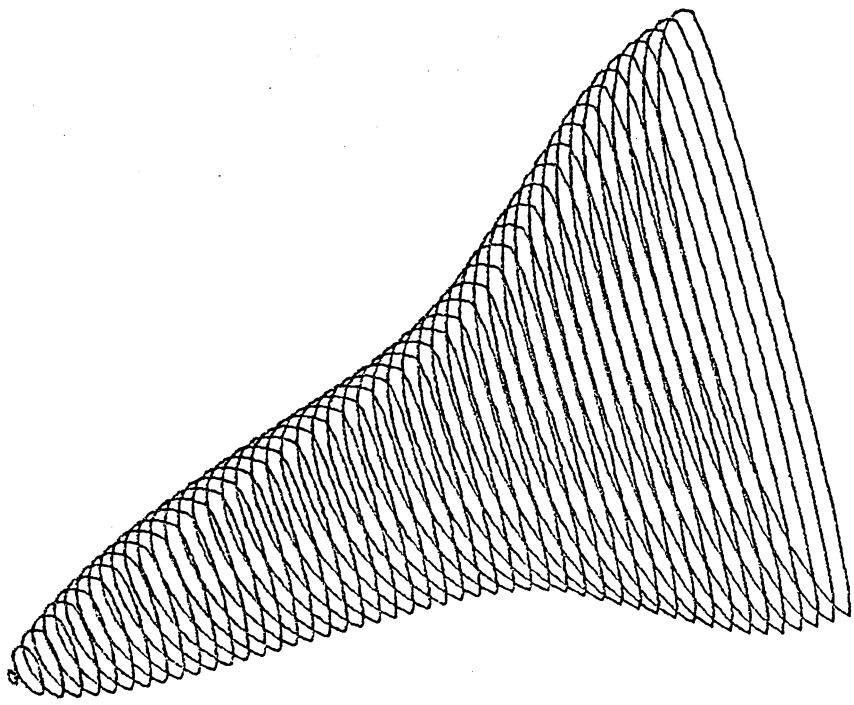

Figure 2: Modified shuttle orbiter geometry using QUICK

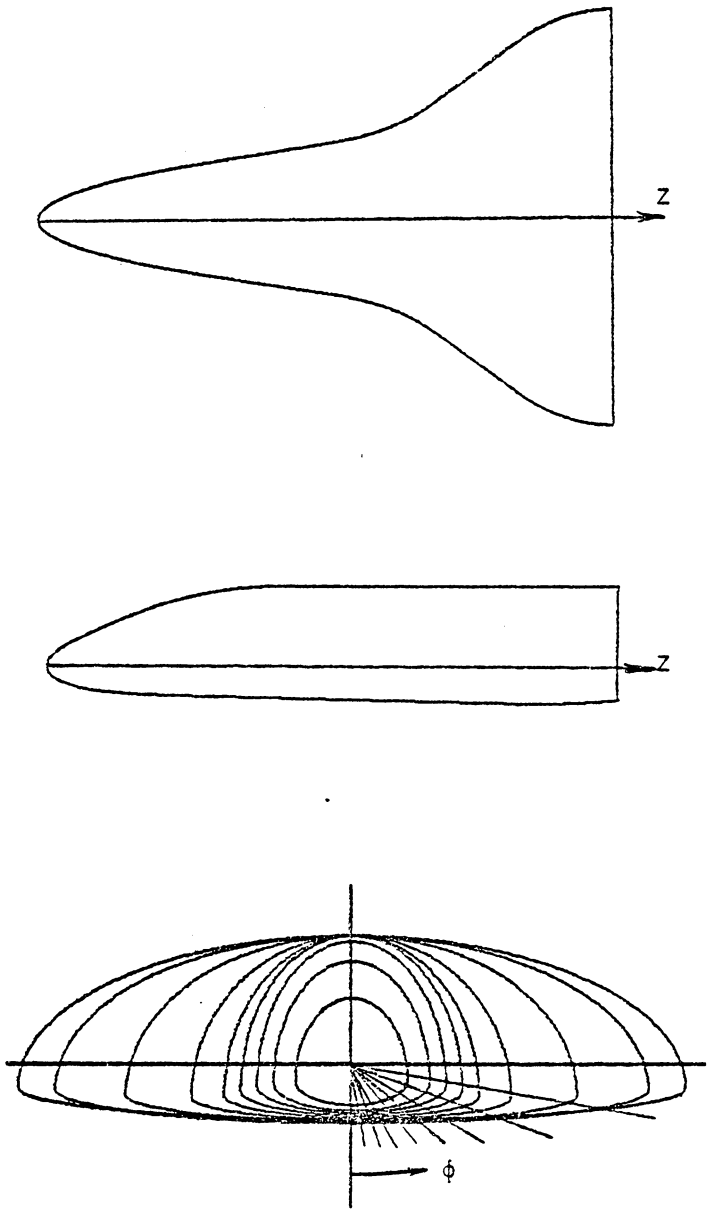


Figure 3: Cross-sections of the modified shuttle orbiter geometry

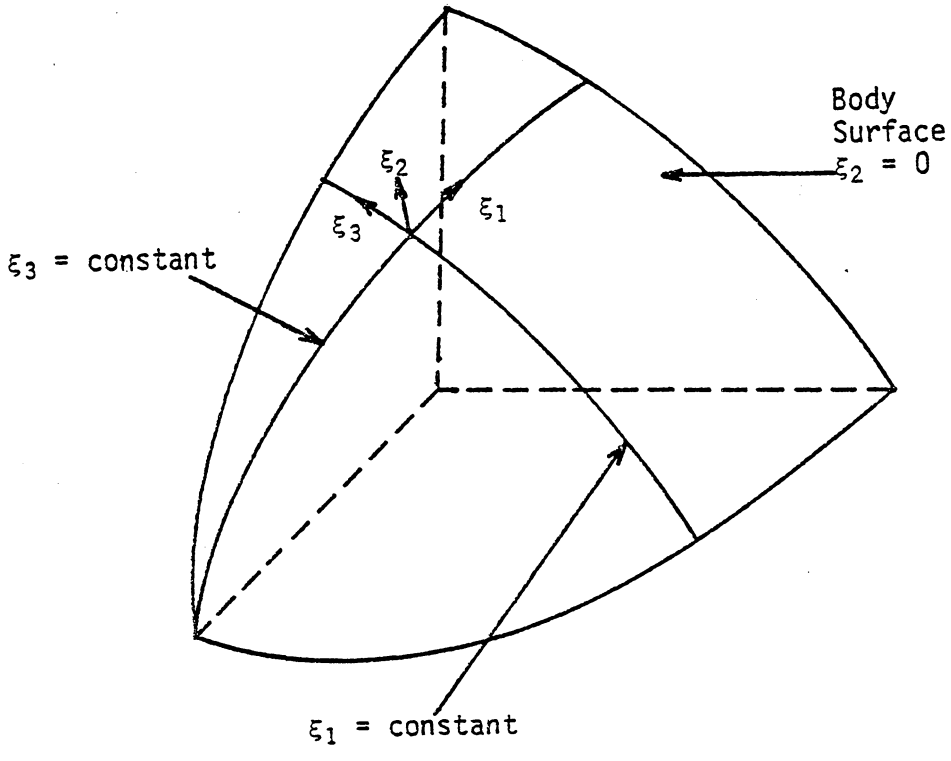


Figure 4: Body coordinate system

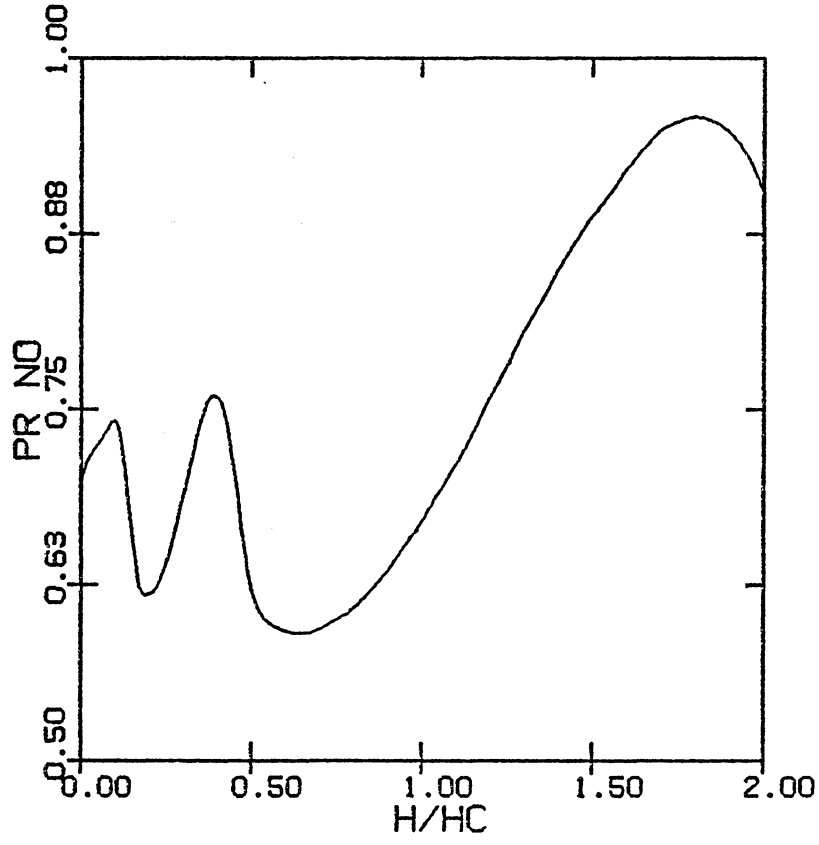


Figure 5: Prandtl number variation with enthalpy for curve-fits

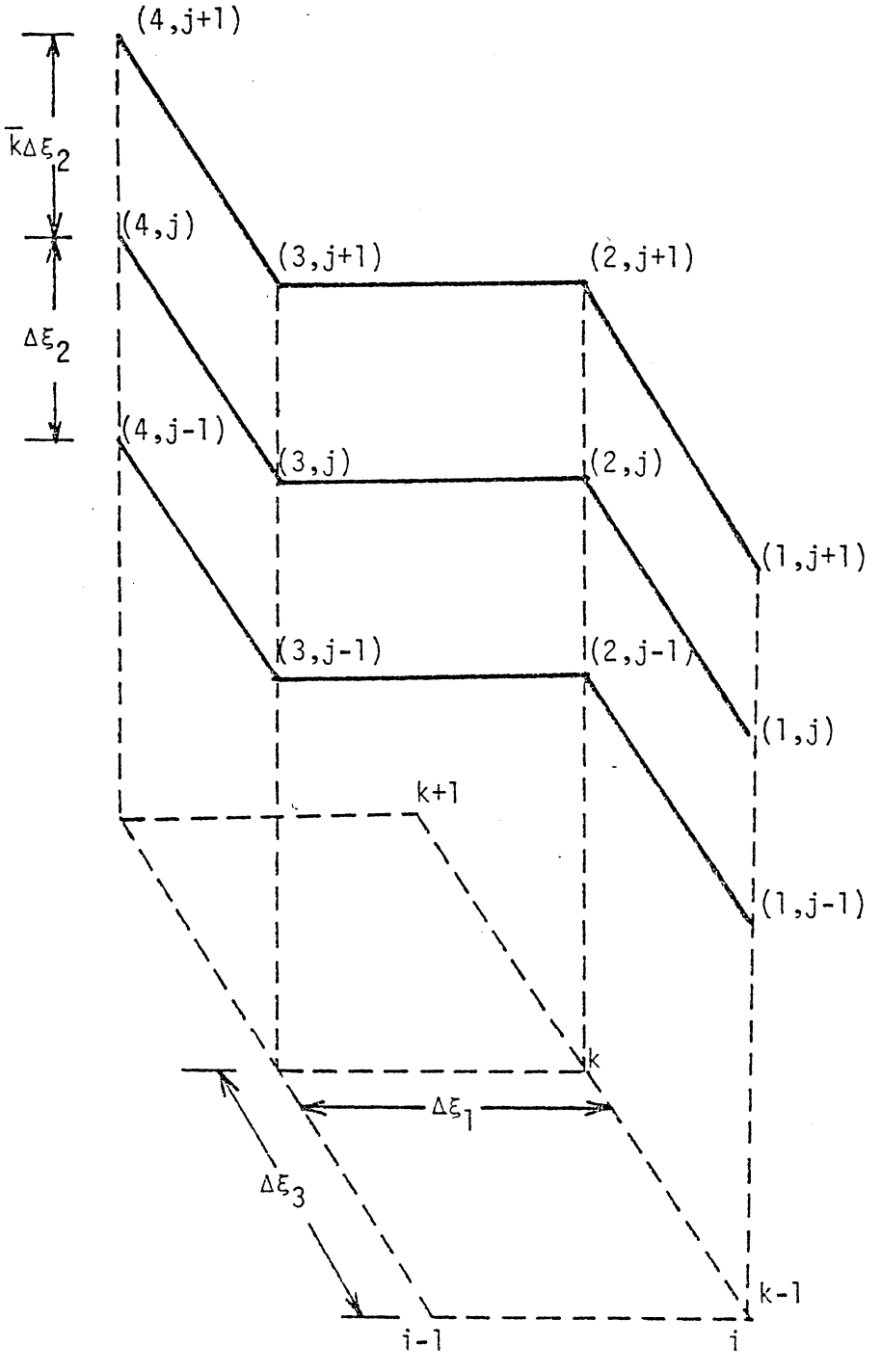


Figure 6: Three-dimensional grid for solution procedure

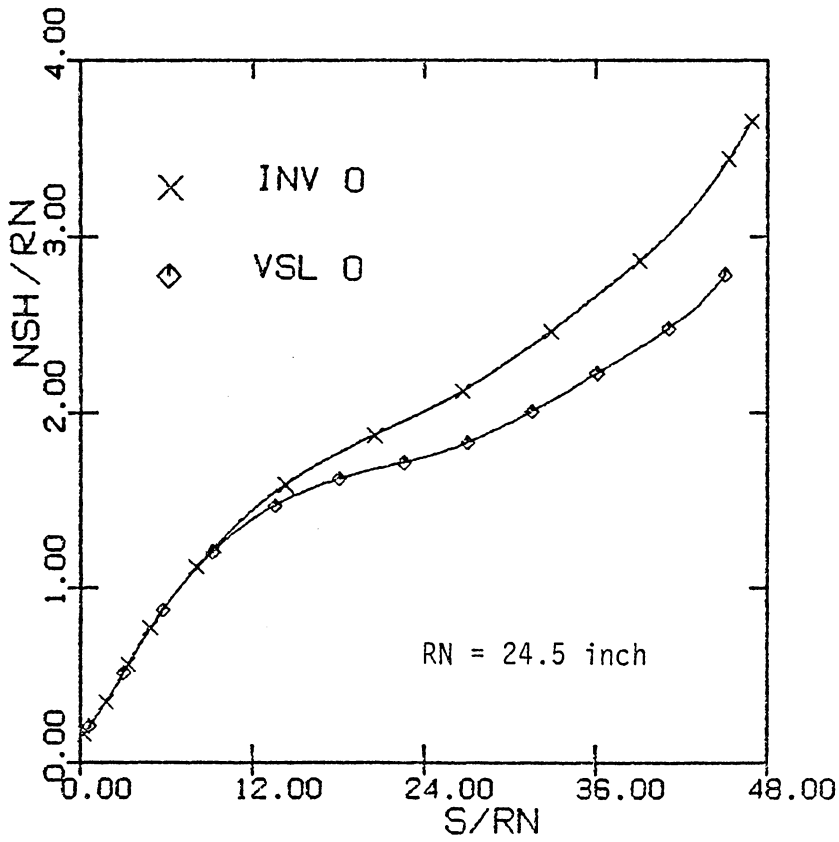


Figure 7: Shock standoff distance for $\phi = 0$ degrees (Case A)

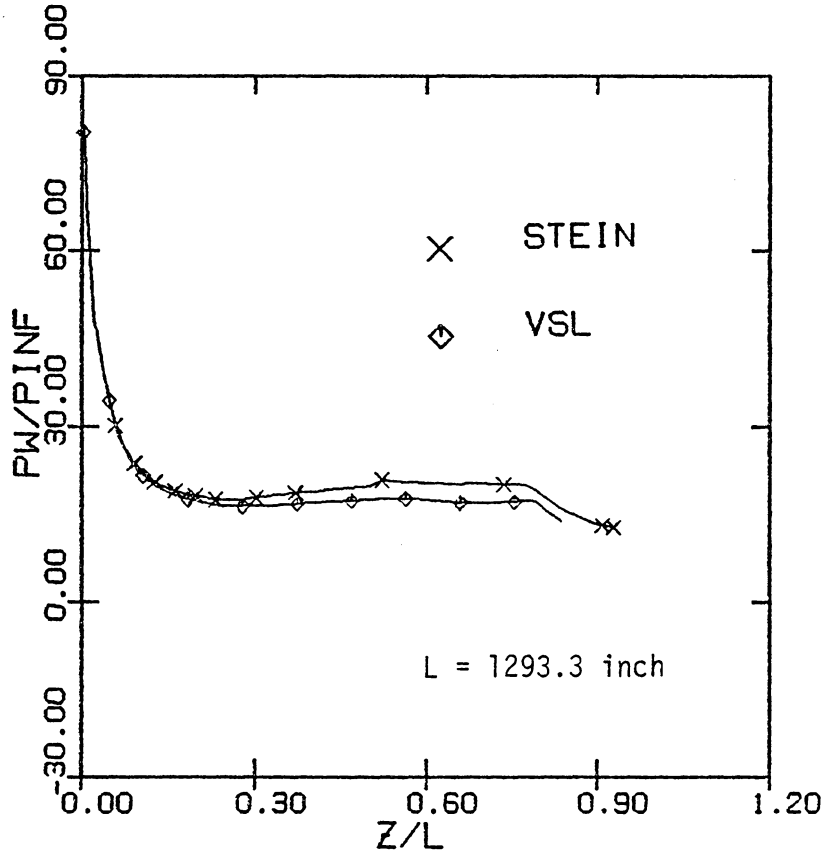


Figure 8: Wall pressure distribution for $\phi$ = 0 degrees (Case A)

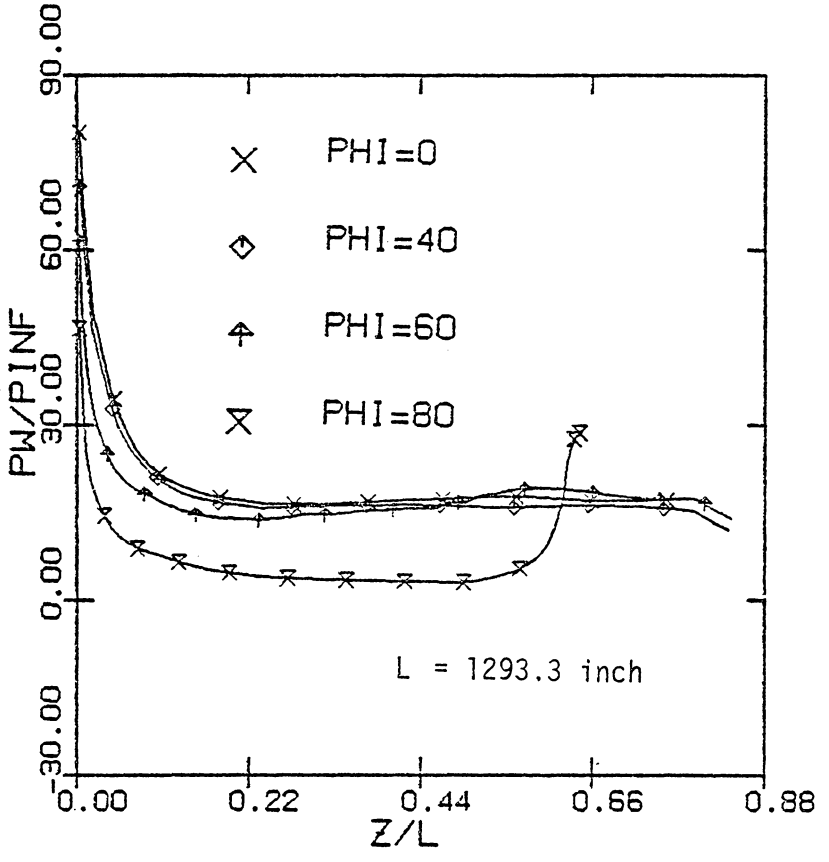


Figure 9: Wall pressure distribution (Case A)

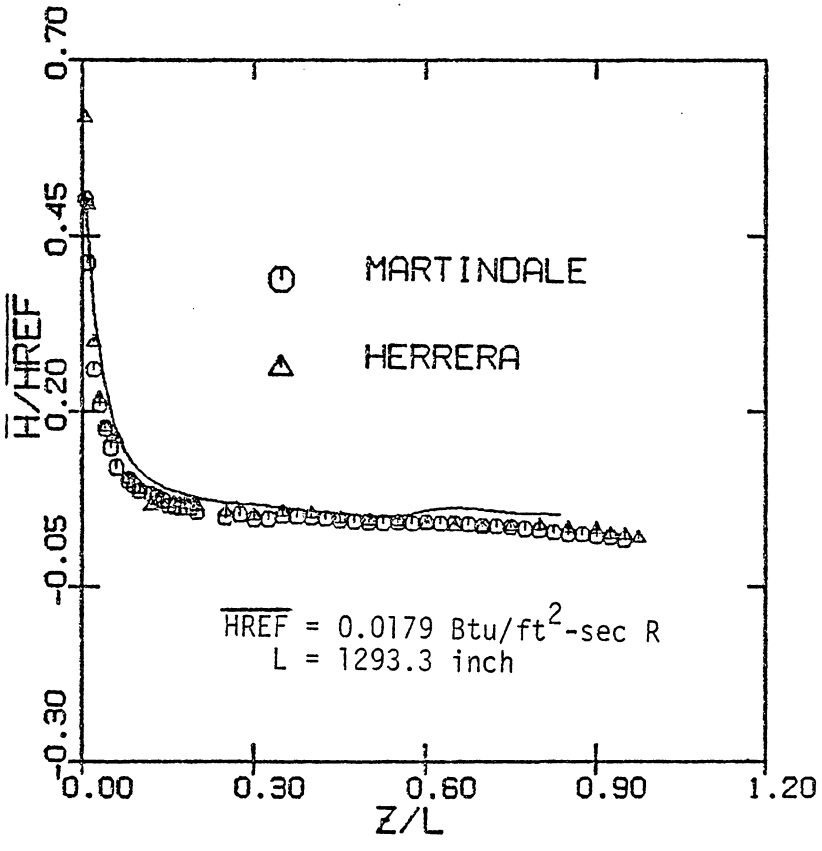


Figure 10: Wall heat-transfer rate for $\phi$ = 0 degrees (Case A)

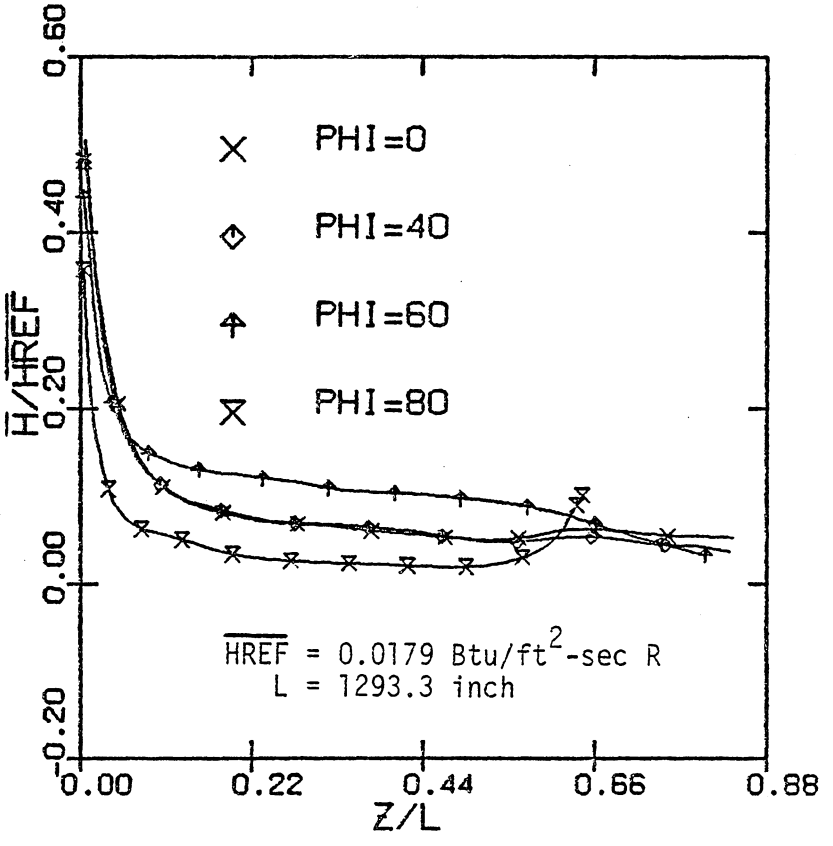


Figure 11: Wall heat-transfer rate (Case A)

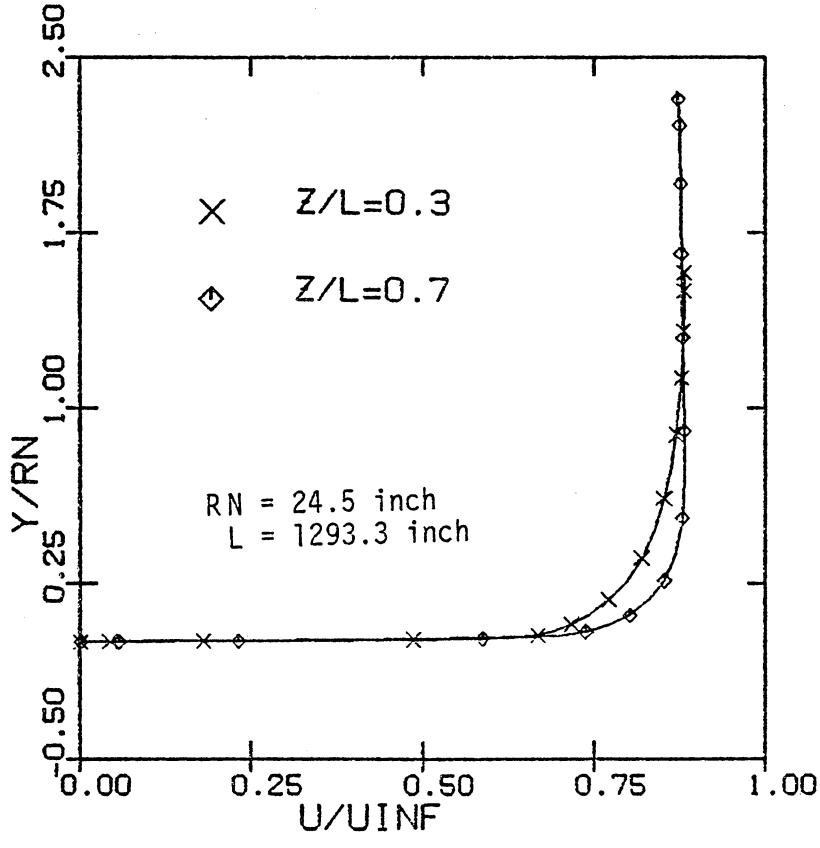


Figure 12: U-velocity profile (Case A)

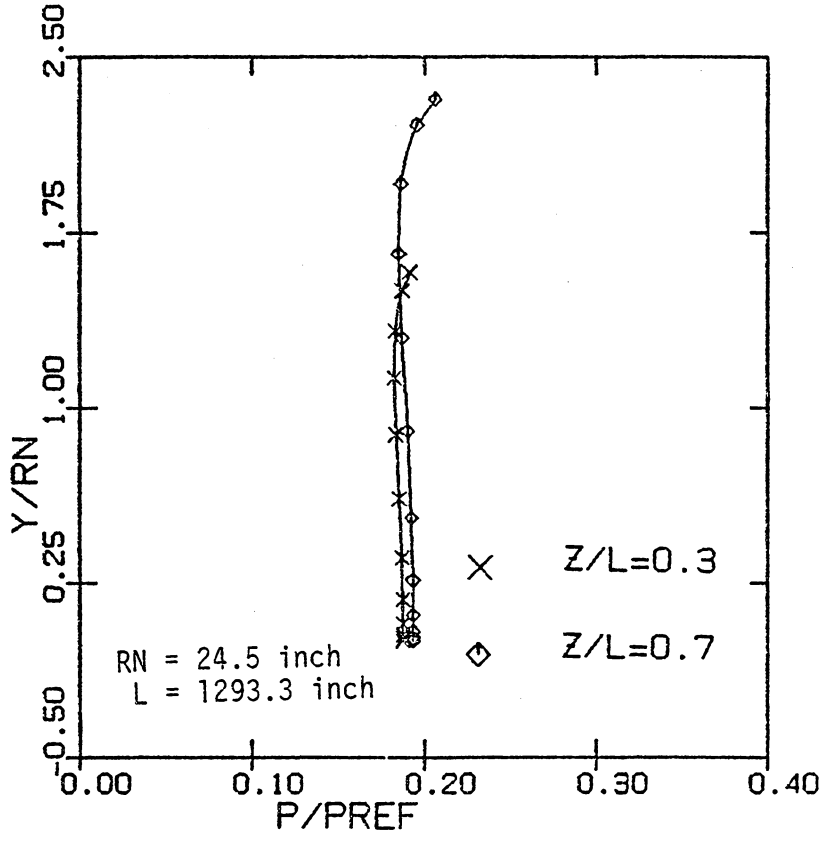


Figure 13: Pressure profile (Case A)

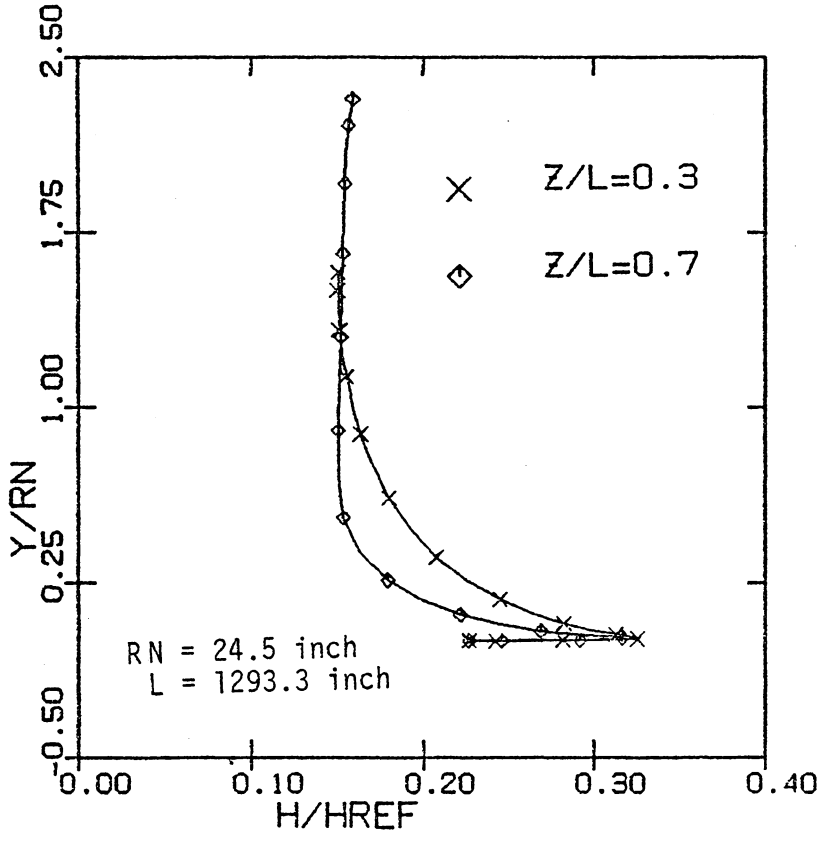


Figure 14: Enthalpy profile (Case A)

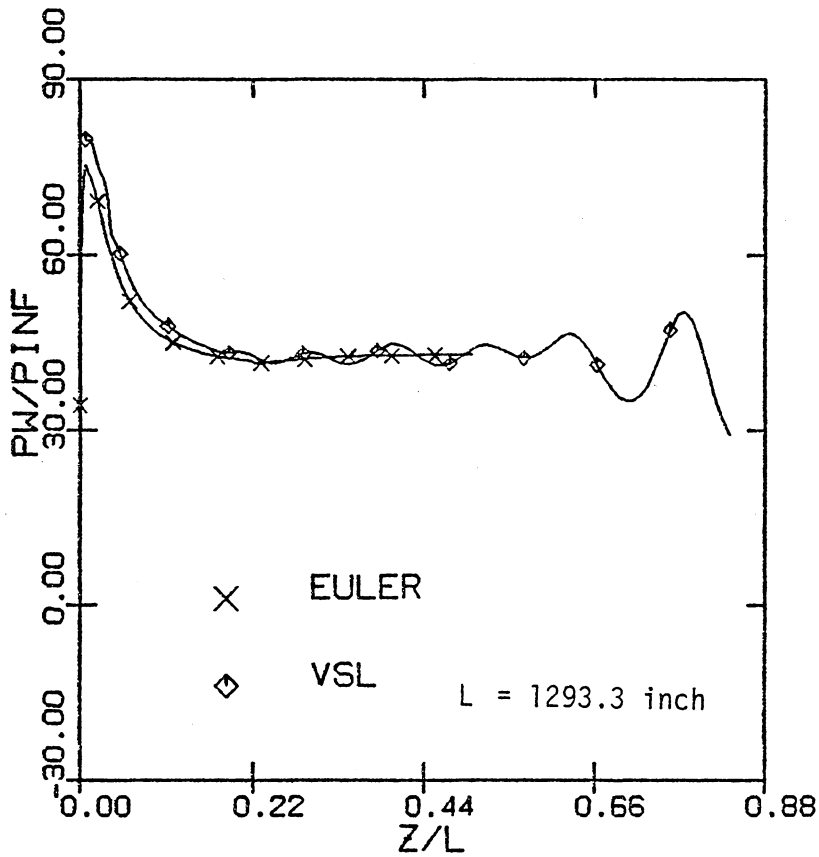


Figure 15: Wall pressure distribution for $\phi$ = 0 degrees (Case B)

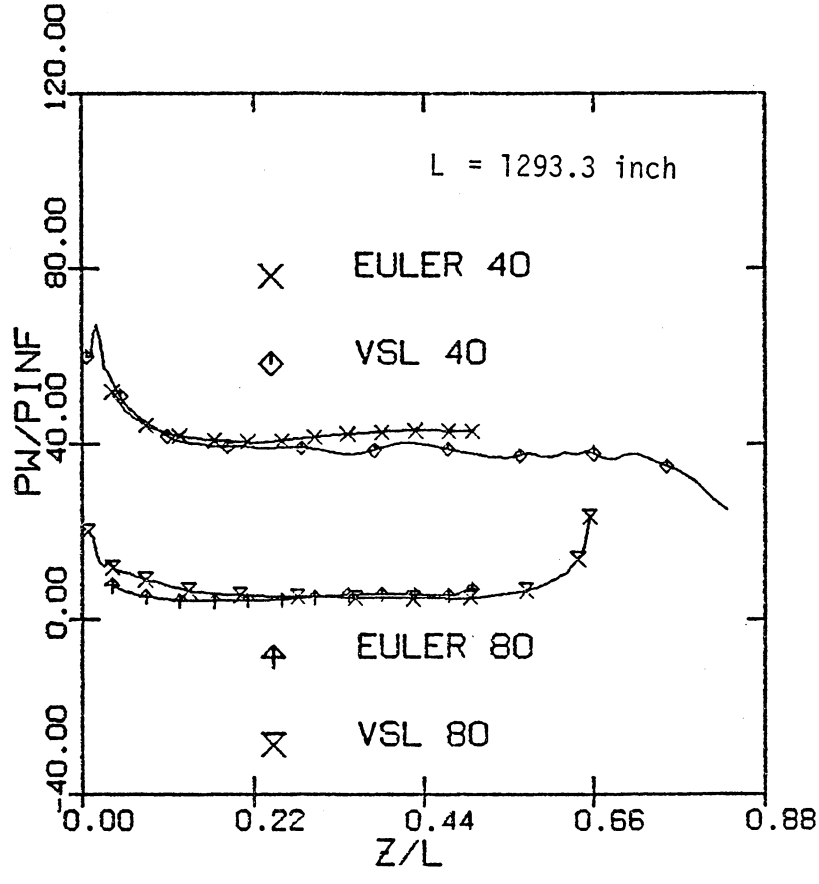


Figure 16: Wall pressure distribution (Case B)

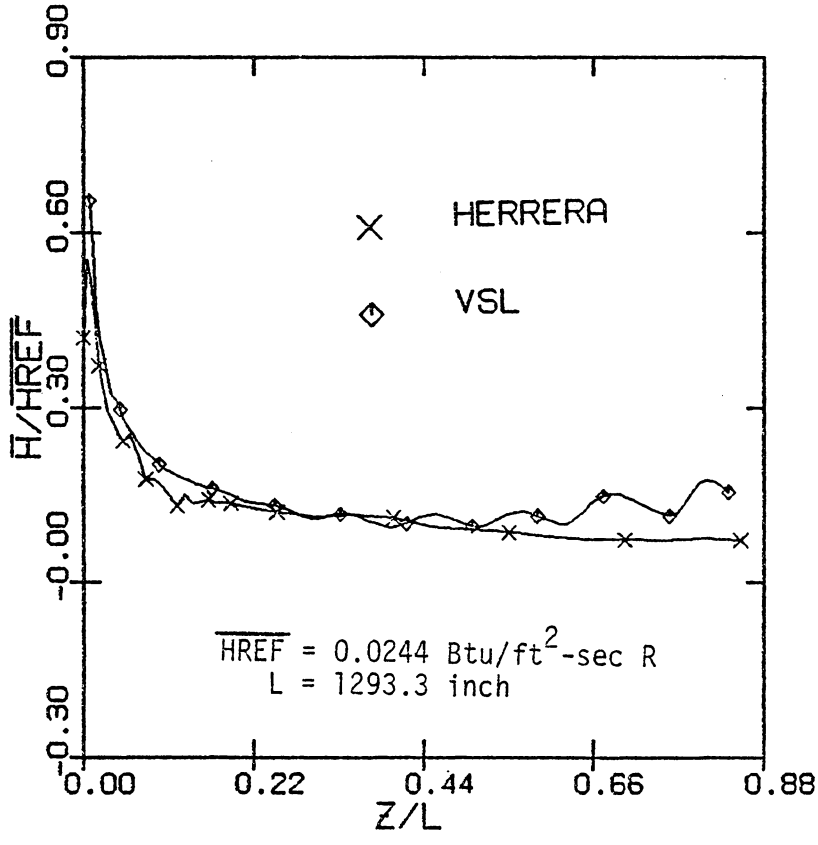


Figure 17: Wall heat-transfer rate for $\phi$ = 0 degrees (Case B)

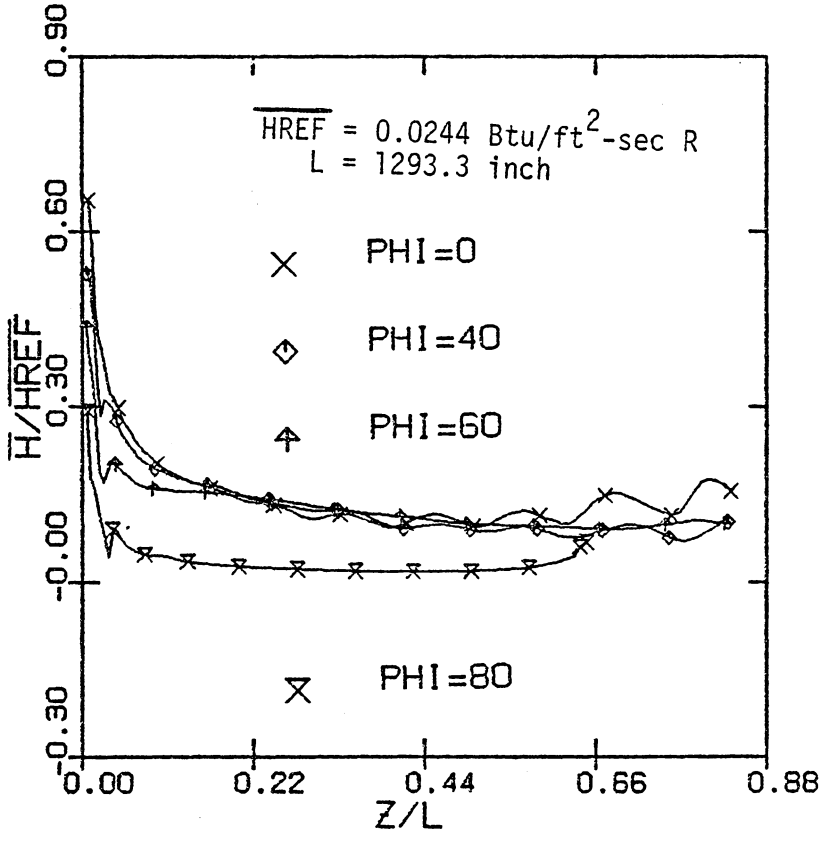


Figure 18: Wall heat-transfer rate (Case B)

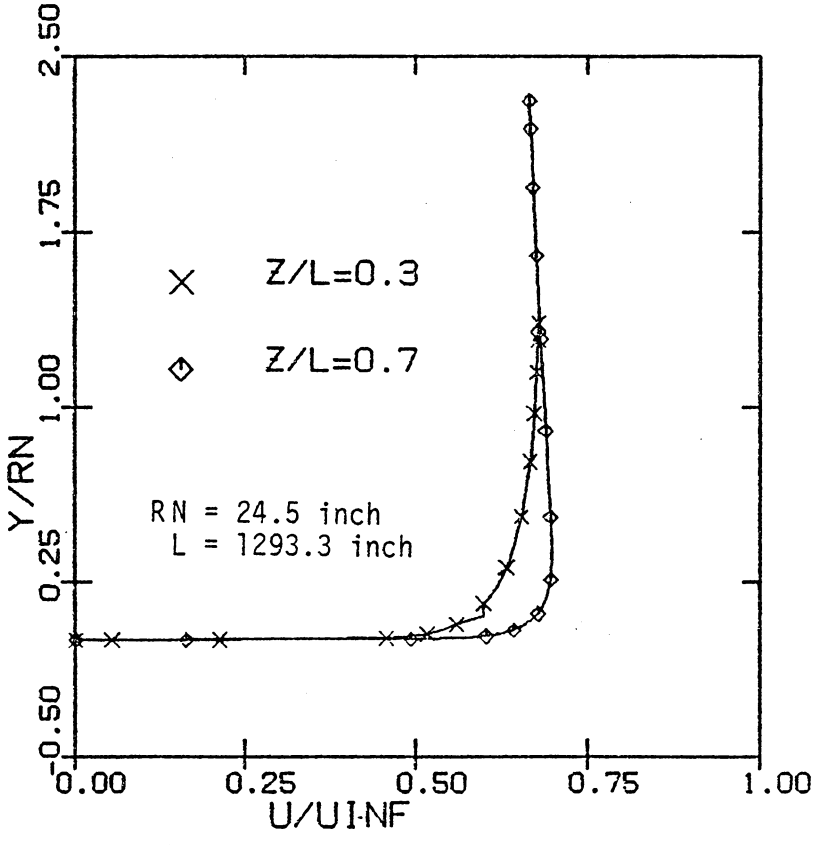


Figure 19: U-velocity profile (Case B)

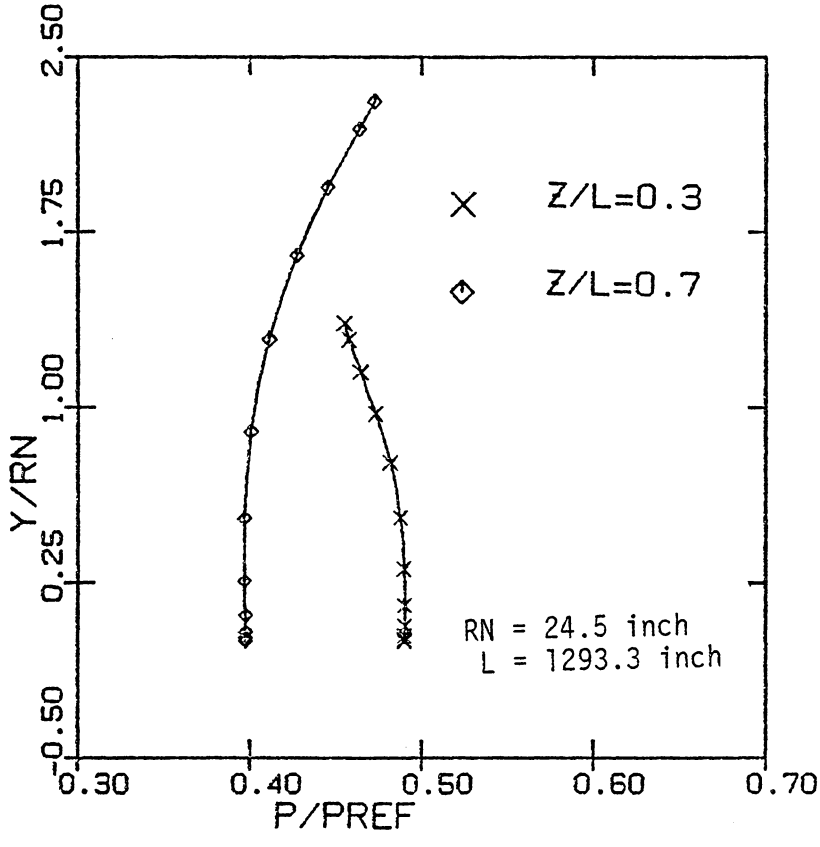


Figure 20: Pressure profile (Case B)

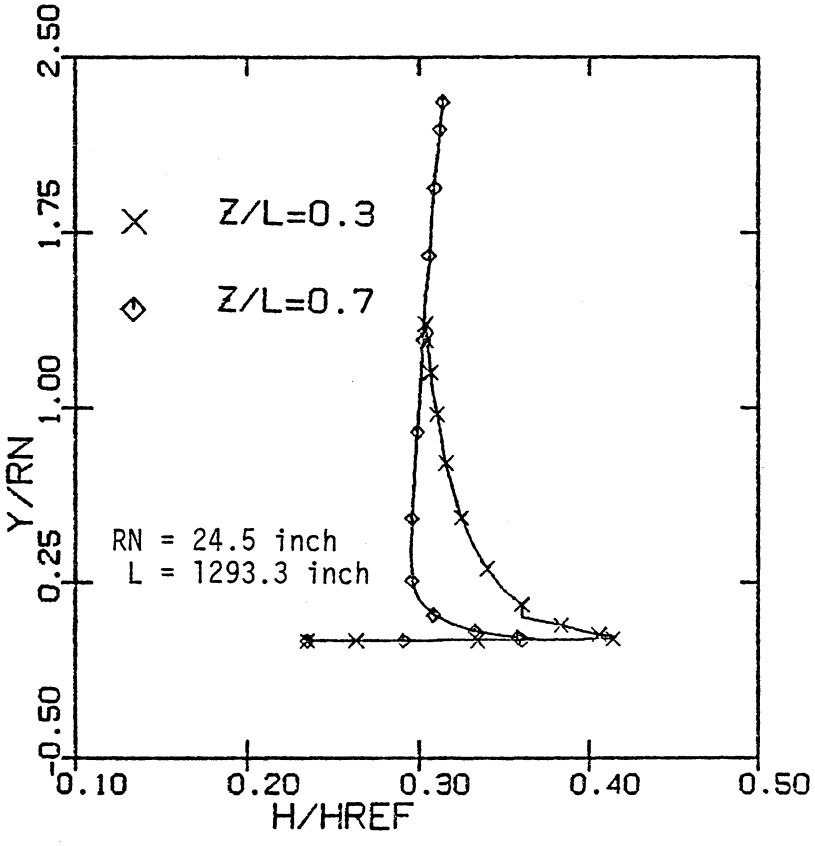


Figure 21: Enthalpy profile (Case B)

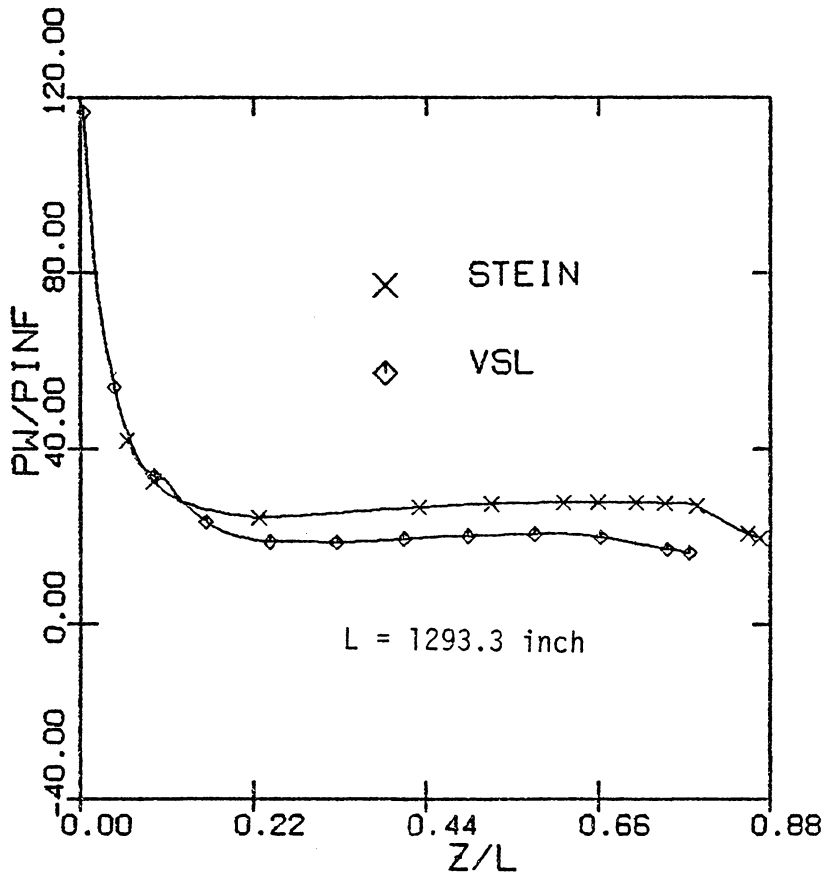


Figure 22: Wall pressure distribution for $\phi$ = 0 degrees (Case C)

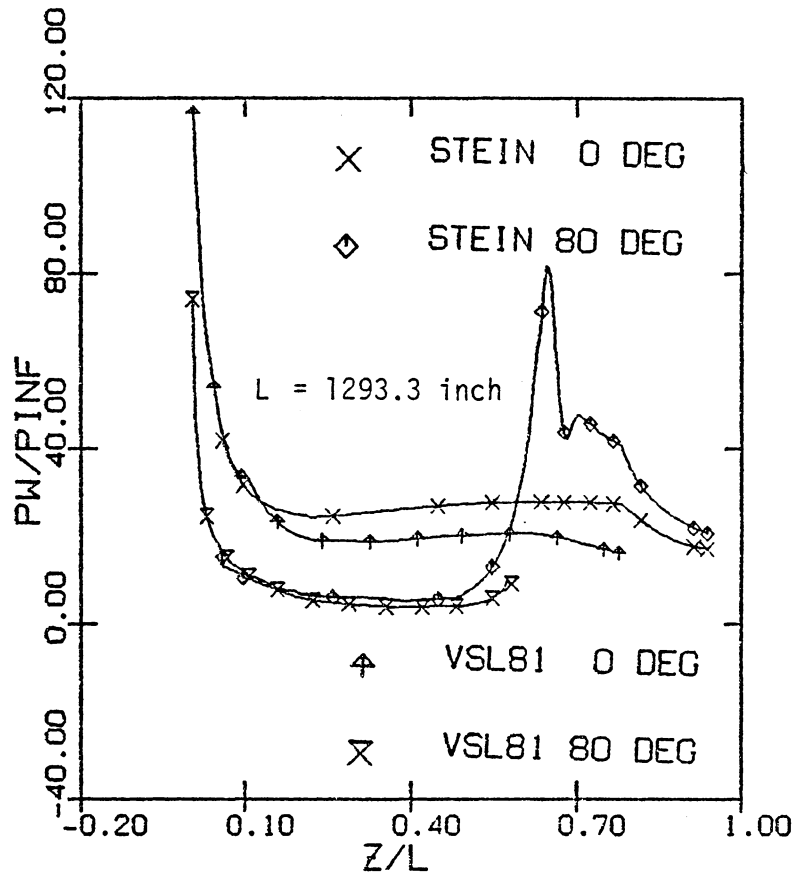


Figure 23: Wall pressure distribution (Case C)

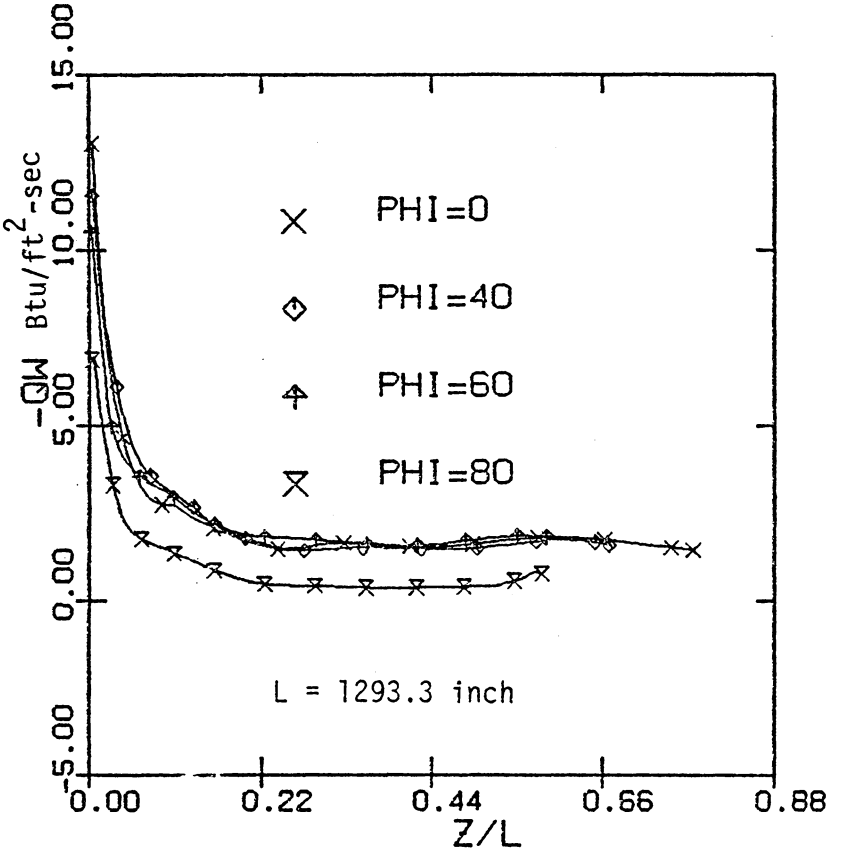


Figure 24: Wall heat-transfer rate (Case C)

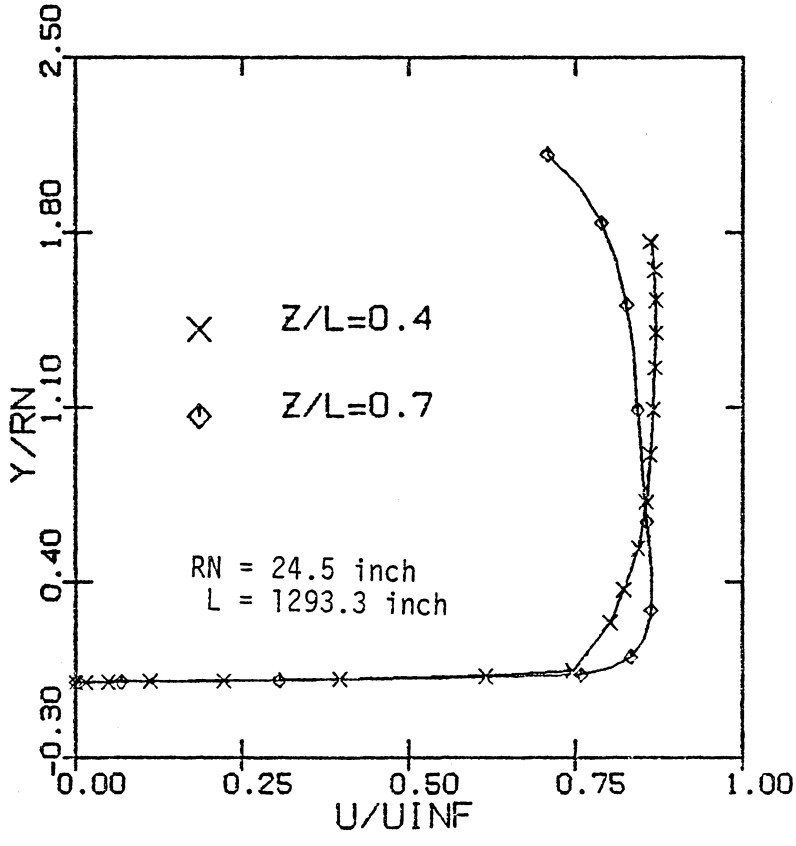


Figure 25: U-velocity profile (Case C)

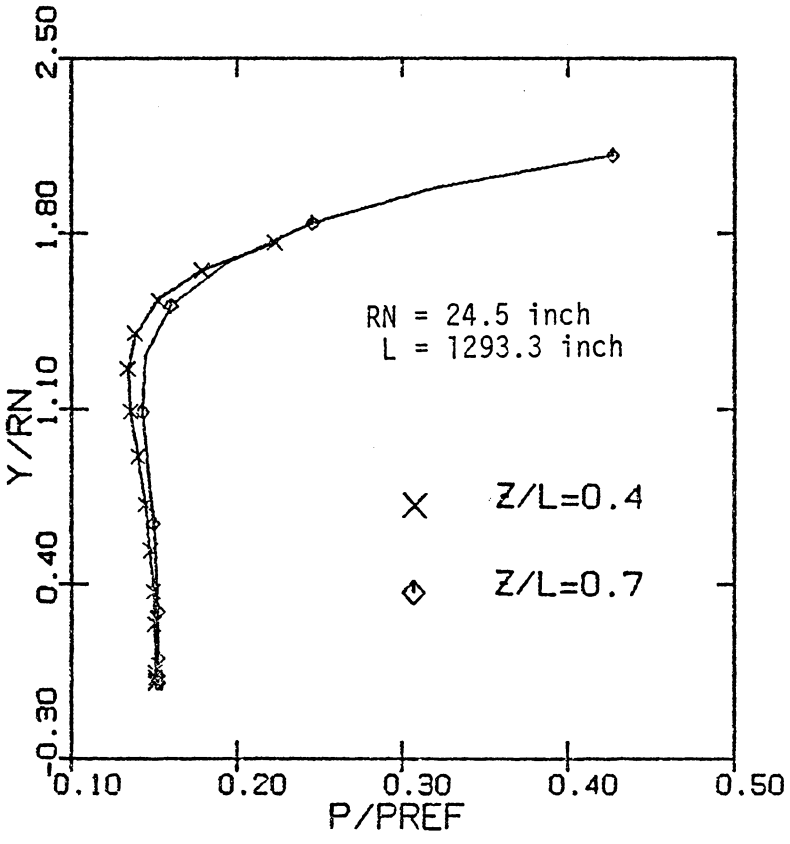


Figure 26: Pressure profile (Case C)

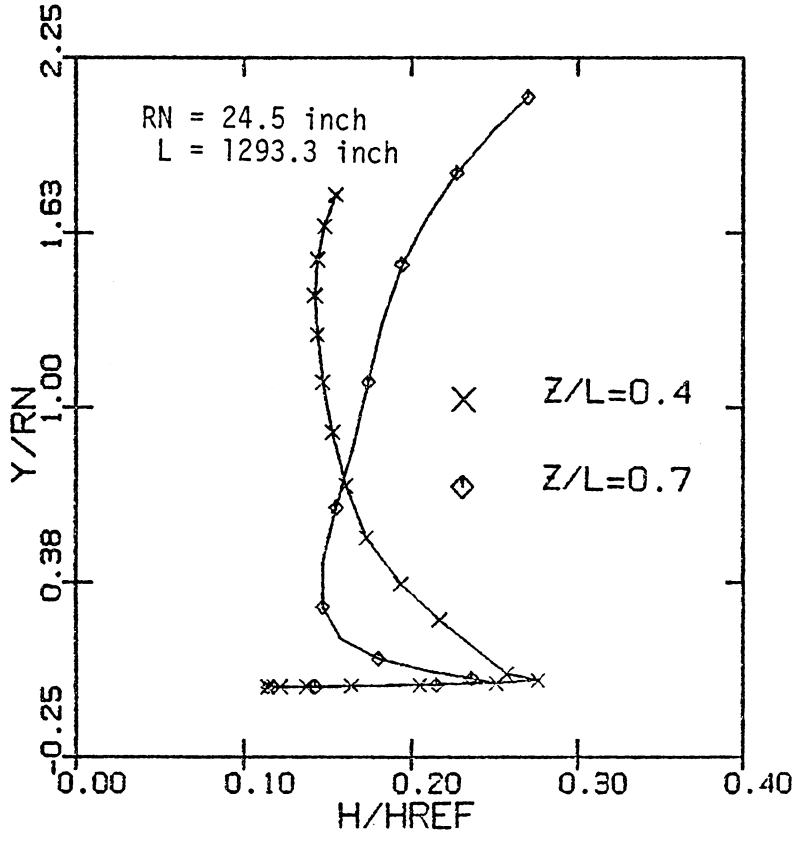


Figure 27: Enthalpy profile (Case C)

**The vita has been removed from the scanned document**